Homogenization of Inconel 718 Made by Additive Manufacturing and Suction Casting

by

Matthew Gargani

B.S. Mechanical Engineering, University of Pittsburgh, 2014

Submitted to the Graduate Faculty of

Swanson School of Engineering in partial fulfillment

of the requirements for the degree of

Master of Science in Materials Science and Engineering

University of Pittsburgh

2019

UNIVERSITY OF PITTSBURGH

SWANSON SCHOOL OF ENGINEERING

This thesis was presented

by

Matthew Gargani

It was defended on

March 26, 2019

and approved by

Brian Gleeson, Ph.D., Professor
Department of Mechanical Engineering and Materials Science

Jung-Kun Lee, Ph.D., Professor
Department of Mechanical Engineering and Materials Science

Wei Xiong, Ph.D., Assistant Professor
Department of Mechanical Engineering and Materials Science

Thesis Advisor: Wei Xiong, Ph.D., Assistant Professor
Department of Mechanical Engineering and Materials Science

Homogenization of Inconel 718 Made by Additive Manufacturing and Suction Casting

Matthew Gargani, MS

University of Pittsburgh, 2019

Inconel 718 is considered a promising candidate for production via additive manufacturing (AM) due to its excellent weldability. However, compared to traditional manufacturing methods, less attention has been paid to developing heat treatments of AM components. To better design the post-processing of Inconel 718 made by AM techniques, the CALPHAD (Calculation of Phase Diagrams) method is applied to study the phase equilibrium, metastable phase behavior, and phase transformations during the homogenization process of Inconel 718. Scanning electron microscopy, energy dispersive X-ray spectroscopy, and electron backscatter diffraction are employed to study the microstructure evolution of different samples supporting the CALPHAD model prediction. Suction cast samples are also investigated to provide a benchmark for comparison. The calculations and experiments are in agreement that homogenization occurs more rapidly in samples made by laser-powder bed fusion than by suction casting. Intriguingly, significant grain growth occurs at the homogenization temperature of 1,180°C for the suction cast samples, but only recrystallization and minor grain growth occurs for the AM samples. AM Inconel 718 samples show promise for reducing the time required for homogenization heat treatment. It is observed that the detrimental Laves phase dissolves in AM samples within 20 minutes due to the smaller grain size and less pronounced Nb segregation than suction cast samples. The new findings confirm that post-processing optimization for AM Inconel 718 components are essential.

Table of Contents

List of Tables

List of Figures

Preface

      The author would like to acknowledge the significant contributions of Yunhao Zhao to this thesis. The experiments presented herein were performed in collaboration with Mr. Zhao and the discussions were developed via working with Mr. Zhao. The author would also like to acknowledge Dr. Wei Xiong for his guidance throughout the research and writing process; Dr. Xiong demonstrated a commitment to his students' growth and success through all of his feedback and suggestions.

1.0 Introduction

Additive manufacturing (AM) methods have the potential to disrupt businesses dominated by traditional subtractive manufacturing methods; however, in order for the full potential of AM to be achieved, significant resources must be devoted to understanding the different microstructural behavior of AM parts and optimizing the mechanical properties of the final AM product. Powder-bed fusion (PBF) has become a leader amongst AM methods due to the ability to create near-net shape complex geometries with minimal wastage of raw material. Inconel 718 is an excellent candidate for PBF due to its excellent weld-ability and preexistence of mass-produced Inconel 718 powder for other powder manufacturing methods (e.g., Hot Isostatic Pressing (HIP)). This research explores the homogenization heat treatment behavior of Inconel 718 parts produced by PBF and by suction casting.

1.1 Additive Manufacturing

As one of the most widely used AM techniques, PBF is capable of building components with complex geometry layer-by-layer [(Das 2003; Kruth et al. 2005; Osakada and Shiomi 2006; Yadroitsev et al. 2010; Gu et al. 2012)], and thus results in less wasted material to create parts and requires less capital investment in tools and dies, which are essential in the conventional subtractive manufacturing processes [(Ma, Wang, and Zeng 2015)]. Additionally, due to extremely high heating and cooling rate, PBF can generate refined grain structures along specific directions [(Amato et al. 2012; Z. Wang et al. 2012; Jia and Gu 2014; Ma, Wang, and Zeng 2015; Strößner,

Terock, and Glatzel 2015; Raghavan et al. 2017)] and hence is able to improve the mechanical properties of materials. Due to having excellent weldability, Ni-based Inconel 718 superalloy is attracting tremendous attention from researchers and engineers as a prime candidate for the PBF process to achieve promising properties. Moreover, because the commercially available Inconel 718 powders developed for HIP operations can be used in PBF, and on account of the high tool wear that Inconel 718 causes in traditional subtractive manufacturing methods [2000_Davis, (Safdar et al. 2013; Ma, Wang, and Zeng 2015; Li et al. 2018; Huang, Chaturvedi, and Richards 1996; Chlebus et al. 2015; X. Wang, Gong, and Chou 2017)], the application values of PBF Inconel 718 are significantly promoted.

1.2 Inconel 718

Inconel 718 is a precipitation-hardenable superalloy with excellent properties at high temperature, such as high strength and exceptional corrosion and creep resistance. The allowable compositions are given in Table 1, with the allowable compositions based on weight percent but in Table 1 are presented also in atomic percent herein for comparison [(ASTM 2018)]. Inconel 718 is stable for utilization up to 650℃, which allows for use in aircraft engines, rocket motors, and nuclear reactors [(Cozar and Pineau 1973; Sundararaman, Mukhopadhyay, and Banerjee 1992; Slama and Abdellaoui 2000; Kuo et al. 2009; Zheng et al. 2012; Beaubois et al. 2004) (Keiser and Brown 1976)]. During the rapid solidification that occurs due to the high cooling rates of PBF, Inconel 718 forms dendrites with segregated microstructure; in the interdendritic zones the nonequilibrium, detrimental Laves phase ($(Ni,Fe,Cr)_2(Nb,Mo,Ti)$, Hexagonal C14) forms [(Keiser and Brown 1976) (Ram et al. 2005; Schneider, Lund, and Fullen 2018)]. The Laves phase usually

2

precipitates during solidification of Inconel 718 due to microsegregation of heavy elements such as Nb and Mo, and causes detrimental effects on the properties of alloys. For instance, the existence of Laves phase can initiate and propagate cracks [(Zhang et al. 2018)] and reduce tensile and stress rupture properties [(Ram et al. 2005)]. In addition, the formation of Laves phase consumes the necessary alloying elements (mainly Nb and Ti) for forming γ'' (Ni_3Nb, BCT $D0_{22}$) and γ' ($Ni_3(Ti,Al)$, FCC $L1_2$), which are the major and minor coherent strengthening phases of Inconel 718, respectively. Therefore, homogenization heat treatments are usually required for the as-solidified samples to dissolve Laves phase and to release Nb and Ti to the matrix to allow for the local composition to be suitable for forming beneficial microstructures, especially the precipitation hardening phases γ'' and γ' during subsequent annealing processes [(Zhang et al. 2015; Trosch et al. 2016; Deng et al. 2017; Popovich et al. 2017; Tucho et al. 2017; Zhang et al. 2018; Huang, Chaturvedi, and Richards 1996; Radhakrishna and Rao 1997; Chlebus et al. 2015; Li et al. 2018)]. γ'' can transform, on overaging, to δ (Ni_3Nb, Orthorhombic $D0_a$), which is detrimental at large phase fractions, but can act as a beneficial grain pinner at low concentrations. Graphics of the crystal structures are provided in Appendix A.

Table 1 - Inconel 718 Allowable Compositions

	Mass [g/mol]	Minimum weight %	Maximum weight %	Minimum atomic % [1]	Maximum atomic % [1]
Ni	58.693	50	55	49.51	54.00
Cr	51.996	17	21	19.00	23.27
Nb	92.906	4.75	5.5	2.97	3.41
Mo	95.95	2.8	3.3	1.70	1.98
Ti	47.867	0.65	1.15	0.79	1.38
Co	58.933	0	1	0.00	0.98
Al	26.982	0.2	0.8	0.43	1.71
Mn	54.938	0	0.35	0.00	0.37
Si	28.085	0	0.35	0.00	0.72
Cu	63.546	0	0.3	0.00	0.27
C	12.011	0	0.08	0.00	0.3838
Fe	55.845	Balance			

Note: (1) The standard maximums and minimums are set by the weight percent. These minimum and maximum atomic percent merely correspond to the listed weight-based compositions. A given composition may have more or less atomic content of any element than the minimum and maximum atomic percent listed here as long as the weight percent is still within the limits.

1.3 Literature Review of Heat Treatments of PBF Inconel 718

Various authors have found that the traditional heat treatments for wrought and cast Inconel 718 are not sufficient for PBF produced Inconel 718 and that the microstructural response to heat treatment is different due to the fine microstructure [(Tucho et al. 2017; Chlebus et al. 2015; Raghavan et al. 2017; Schneider, Lund, and Fullen 2018)]. Zhang et al. found that homogenization + solutionizing + aging (HSA) heat treatment in cast samples left Laves phase, coarse δ phase, and pores in the matrix in addition to beneficial γ' and γ'' phases; whereas HSA heat treatment in PBF samples left only very fine δ phase and a few carbides in the matrix in addition to γ' and γ'' phases [(Zhang et al. 2018)]. It is also suggested that although HSA treated PBF samples are more ductile than HSA treated cast samples, the PBF samples precipitate too much δ phase and would benefit from a shorter solutionizing heat treatment than the cast samples [(Zhang et al. 2018)]. Chlebus et al. found that PBF samples required a higher homogenization heat treatment than that prescribed for wrought or cast Inconel 718 samples [(Chlebus et al. 2015)]. Schneider et al. found that PBF samples could achieve specified heat-treated wrought mechanical properties with reduced heat treatment steps, and that the recrystallization behavior of PBF samples differed from cast samples [(Schneider, Lund, and Fullen 2018)]. These findings demonstrate that additional work is needed to develop optimal heat treatments for Inconel 718 parts produced by PBF.

While various investigations into the effect of heat treatment on PBF parts of Inconel 718 have been performed [(Zhang et al. 2018, 2015; Deng et al. 2017; Popovich et al. 2017; Tucho et al. 2017; Chlebus et al. 2015; Trosch et al. 2016; Raghavan et al. 2017; Ma, Wang, and Zeng 2015; Amato et al. 2012; Z. Wang et al. 2012; Li et al. 2018)], very few studies into the microstructural evolution of Inconel 718 during homogenization heat treatment following PBF have been performed. Meanwhile, even for the traditional wrought and cast Inconel 718 parts, the same topic

is not well studied yet. Such lack of investigation on the homogenization processes poses obstacles to the development of an optimal post-processing design. It is thus obvious that a systematic study is necessary to gain better understanding of microstructural evolution during homogenization heat treatment for Inconel 718 alloys. The work herein compares the effect of homogenization heat treatment on samples produced by casting and by PBF with particular attention paid to the Nb homogeneity evolution and recrystallization behavior at various times under a homogenization heat treatment. CALPHAD-based (Calculation of Phase Diagrams) computational thermodynamics and kinetics is utilized to design the homogenization temperature and time. The samples were examined by Scanning Electron Microscope (SEM), Electron Backscatter Diffraction (EBSD), and Energy-Dispersive Spectroscopy (EDS) to characterize the phase transformation and recrystallization behaviors during homogenization processes.

2.0 Method

Computational and experimental methods are used to explore the homogenization heat treatment behavior of cast and AM samples. The computational work guided the choice of experimental parameters, and the experimental results provided input to further computational work. The interaction of computation and experiment is utilized in order to optimize the conclusions that are able to be drawn from the results.

2.1 Computation

The following types of computations are performed:

- Determination of time to heat sample in furnace;

- Phase diagram;

- Scheil diagram;

- Step diagram;

- Diffusion simulation.

Excel is used for the time-to-temperature calculation, and Thermo-Calc is used for all of the thermodynamic calculations.

2.1.1 Theory

2.1.1.1 Temperature Transients

In order to verify that the samples analyzed reach the homogenization heat treatment temperature in a negligible amount of time, a thermal analysis is performed. The thermal mass of the sample is:

$$m_{th} = (\rho V)c_p \tag{1}$$

where m_{th} is the thermal mass of the sample, ρ is the density of the sample, V is the volume of the sample, and c_p is the specific heat capacity of the sample. c_p can be determined from thermodynamic quantities and does not need to be assumed:

$$c_p = \frac{dh}{dT}\bigg|_P = -T\left(\frac{d^2G}{dT^2}\right)_P \tag{2}$$

where $\frac{dh}{dT}\big|_P$ is the change in enthalpy with respect to temperature at constant pressure, T is the temperature, and $\left(\frac{d^2G}{dT^2}\right)_P$ is the second derivative of the Gibbs free energy with respect to temperature at constant pressure.

The rate of temperature increase of the sample is:

$$\frac{dT}{dt} = \frac{dq}{dt} * \frac{1}{m_{th}} \tag{3}$$

where $\frac{dT}{dt}$ is the time rate of temperature increase in the sample and $\frac{dq}{dt}$ is the time rate of heat flow into the sample. In general, heat can flow via conduction, convection, or radiation. Thus the heat flow is:

$$\frac{dq}{dt} = -kA_{cond}(\nabla T) + hA_{conv}(T_{furnace} - T_{sample})$$

$$+ \epsilon\sigma A_{rad}\left(T_{furnace}^4 - T_{sample}^4\right)$$

(4)

where k is the effective conductivity between the sample and the furnace, ∇T is the spatial gradient in the temperature, h is the convective temperature coefficient of natural convection in the furnace, $T_{furnace}$ is the temperature of the furnace (1,180°C, or 1453.15 K), T_{sample} is the temperature of the sample, ϵ is the emissivity of the sample, and σ is the Stefan-Boltzmann constant $\left(5.670 * 10^{-8}\frac{W}{m^2K^4}\right)$, and A_i is the area of the sample available for heat transfer for each form of heat transfer.

2.1.1.2 Equilibrium Thermo-Calc

In this work, thermodynamic (TCNI8) and mobility (MOBNI4) databases released by the Thermo-Calc software AB [(Chen et al. 2016)] have been adopted to understand phase equilibria and phase transformations in Inconel 718 during homogenization processes. In the thermodynamic database, all phases are modeled using the compound energy formalism (CEF) [(Hillert 2001)]. The Gibbs free energy of liquid and solid solution phases are modeled using the substitutional solution model, whereas the modeling of Gibbs free energy of intermetallic phases such as Laves phase, δ, and γ" phases uses the sublattice model [(J. O. Andersson et al. 2002; Division and Metallurgy 1981)]. For example, for a binary system (e.g. A-B), the molar Gibbs free energy of a solid solution phase ϕ can be described as:

$$G_m^\phi = \sum_i x_i \,{}^oG_i^\phi + RT \sum_i x_i ln x_i + G_{ex}^\phi$$

(5)

where the first term on the right side represents the reference state of Gibbs free energy and the second term indicates the contribution of configurational entropy to the Gibbs free energy, where i is the number of components in ϕ, x_i is the mole fraction of component i, ${}^oG_i^\phi$ is the Gibbs free energy of pure component i in ϕ, R is the gas constant, and T is the temperature. The third term G_{ex}^ϕ is the excess Gibbs free energy of mixing, which can be expressed by Redlich-Kister polynomial [(Redlich and Kister 2005)] as:

$$G_{ex}^\phi = x_A x_B \sum_v {}^v L_{A,B} (x_A - x_B)^v \tag{6}$$

where x_A and x_B are the mole fraction of component A and B, respectively; ${}^v L_{A,B}$ is the interaction coefficient and v is the power. It should be noted that if $v = 0$, the model becomes a regular solution model, while when $v = 1$, it becomes a sub-regular solution model. The parameters are optimized by fitting the model with experimental thermodynamic data.

As for an intermetallic phase ϕ, the Gibbs free energy is described by considering the interactions between various sublattices. As the simplest case, a two-sublattice model, i.e. $(A, B)_m (A, B)_n$ gives [(Wu et al. 2012)]

$$
\begin{aligned}
G_m^\phi = & \sum_i \sum_j y_i' y_j'' \, {}^oG_{i:j}^\phi \\
& + RT \left(\frac{m}{m+n} \sum_i y_i' \ln(y_i') + \frac{n}{m+n} \sum_i y_i'' \ln(y_i'') \right) \\
& + y_A' y_B' \sum_j y_i'' \, {}^v L_{A,B:j} (y_A' - y_B')^v \\
& + y_A'' y_B'' \sum_j y_i' \, {}^v L_{i:A,B} (y_A'' - y_B'')^v \\
& + y_A' y_B' y_A'' y_B'' L_{A,B:A,B}
\end{aligned}
\tag{7}
$$

On the right side of eq. (7) and similarly to the expression of substitutional solution model, the first term in the expression of sublattice model represents the reference state of Gibbs free energy and the second term indicates the contribution of configurational entropy to the Gibbs free energy. The summation of the last three terms is the excess Gibbs free energy. $^oG_{i:j}^\phi$ is the Gibbs free energy of "end members", which are the stoichiometric compounds consisted of constituents of each sublattice [(Saunders and Miodownik 1998)]; m and n are the ratio of sites on each sublattices, y_i' and y_i'' represents the mole fraction of component i in the first and second sublattices, respectively; L is coefficients of interaction between the sublattices.

After establishing the thermodynamic description of binary system, one can extend the excess Gibbs free energy model to a higher order multicomponent system, of which the descriptions of excess Gibbs free energy are extrapolated using the geometrical Muggianu method [(Muggianu, Gambino, and Bros 1975)]. More detailed discussion about the models of Gibbs free energy can be found in [(Lukas, Fries, and Sundman 2007)].

2.1.1.3 Kinetic Thermo-Calc (Scheil Calculation)

Scheil diagrams are based on simplified kinetic solidification simulations. The two major simplifying assumptions are:

1. The liquid phase is fully homogenized in both temperature and compositions;

2. The solid phases have no diffusion.

Based on these assumptions, the Gibbs free energy (GFE) is calculated for each phase at each temperature as the temperature approaches 0 K. As equilibrium solid phase is calculated, it is removed from the system and the reduced liquid is then at a new composition. This method is fairly accurate for systems with rapid cooling and little time for solid diffusion. These assumptions

11

allow for relatively quick simulations that can predict non-equilibrium structures due to solidification phenomena.

2.1.1.4 Kinetic Thermo-Calc (Diffusion)

The kinetic modeling was performed in the diffusion module (DICTRA) implemented in Thermo-Calc using both the TCNI8 and MOBNI4 databases. In DICTRA, the flux of a component k along the Z direction in the volume-fixed frame of reference is described as:

$$J_k = -\sum_{i=1}^{n} L'_{ki} \frac{\partial \mu_i}{\partial z} \qquad (8)$$

where $\frac{\partial \mu_i}{\partial z}$ is the chemical potential of component i along the Z direction in the system. L'_{ki} is a matrix of kinetic coefficients and is given by:

$$L'_{ki} = \sum_{j=1}^{n} (\delta_{jk} - c_k V_j) L_{ji} \qquad (9)$$

where δ_{jk} is the Kronecker delta and $\delta_{jk} = 1$ when $j = k$, and $\delta_{jk} = 0$ otherwise. V_j is the partial molar volume of element j and c_k is the concentration of k. L_{ji} is a function of the atomic mobility of component k.

Since it is usually more convenient to use the concentration gradient in the expression of flux rather than the chemical potential, the chain rule of derivation is applied to eq. (9) and then gives:

$$J_k = -\sum_{i=1}^{n} L'_{ki} \sum_{j=1}^{n} \frac{\partial \mu_i}{\partial c_j} \frac{\partial c_j}{\partial z} \qquad (10)$$

12

if we rewrite eq. (10) as:

$$J_k = -\sum_{i=1}^{n} D_{kj} \frac{\partial c_j}{\partial z} \qquad (11)$$

By comparing eq. (10) and eq. (11), one can get:

$$D_{kj} = \sum_{i=1}^{n} L'_{ki} \frac{\partial \mu_i}{\partial c_j} \qquad (12)$$

where D_{kj} is the matrix of chemical diffusivity of element k. Because L'_{ki} is related to the atomic mobility of k and $\frac{\partial \mu_i}{\partial c_j}$ is a thermodynamic factor, the diffusivity in DICTRA is therefore consisted of one thermodynamic part and one kinetic part. In MOBNI4 database, the atomic mobilities assessed by experimental data are stored to reduce the number of parameters in the database. Hence, when performing kinetic simulation, the mobility and thermodynamic factors from both kinetic and thermodynamic databases will be invoked by DICTRA to generate the matrix of chemical diffusivity D_{kj} and the description of the flux J_k can be immediately obtained from eq. (11). As a result, the concentration change of component k with respect to the time and distance can be solved according to Fick's second law:

$$\frac{\partial c_k}{\partial t} = \frac{\partial}{\partial z}(-J_k) \qquad (13)$$

More detailed and comprehensive discussion about the diffusivity theory employed in DICTRA can be found in the work of Andersson and Ågren [(Jan Olof Andersson and Ågren 1992)].

2.1.2 Inputs

2.1.2.1 Temperature Transient

Although Equation (4) describes the three ways that heat can be transferred – conduction, convection, and radiation – the samples analyzed herein are encapsulated into vacuumed quartz tubes back-filled with pure Argon gas, and are thus insulated from conduction and convection from the furnace. Most of the heat transfer will therefore occur by radiation, but conduction and convection can be conservatively ignored. Equation (4) thus simplifies to:

$$\frac{dq}{dt} = \epsilon \sigma A_{rad}\left(T_{furnace}^4 - T_{sample}^4\right) \tag{14}$$

and combining Equations (14) and (3) gives

$$\frac{dT}{dt} = \epsilon \sigma A_{rad}\left(T_{furnace}^4 - T_{sample}^4\right) * \frac{1}{-V\rho T \left(\frac{d^2 G}{dT^2}\right)_P} \tag{15}$$

For metals, emissivity depends on the surface finish. Fluke Process Instruments list emissivity values for Inconel ranging from 0.2-0.5 in the polished condition, with other conditions listing higher values; for this analysis 0.2 is conservatively used [(Fluke Process Instruments 2019)]. The Stefan-Boltzman constant is $5.67 \times 10^{-8} \frac{W}{m^2 K^4}$. For a sample of size 5 mm x 5 mm x 10 mm, the surface area (A_{rad}) is equal to 0.00025 m². The temperature of the furnace is assumed to be a constant 1,453.15 K (1,180°C). The initial temperature of the sample is assumed to be 298.15 K (25°C). For a sample of size 5 mm x 5 mm x 10 mm, the volume (V) is equal to 0.25×10^{-6} m³. The density (ρ) and $\left(\frac{d^2 G}{dT^2}\right)_P$ are calculated via Thermo-Calc using the composition given in Table 2. The results of the Thermo-Calc calculation are presented in the Results Section.

Table 2 - Composition for Temperature Transient Calculation

Element:	Ni	Cr	Fe	Nb	Mo	Al	Ti	C
Atomic Percent	51.0162	21.86	19.07	3.25	1.92	1.26	1.24	0.3838
Weight Percent	51.8	19.66	18.42	5.22	3.19	0.59	1.03	0.080

2.1.2.2 Phase Diagram

Two phase diagrams are calculated using Thermo-Calc. One phase diagram shows the equilibrium phases of the AM samples with the hypothetical maximum carbon content (AM_MaxC), while the second phase diagram shows the equilibrium phase diagram of a Ni-Cr-Fe-Nb alloy. Both phase diagrams vary the content of Ni and Nb while holding all other contents constant. Both diagrams vary from 0 to 20 atomic percent Nb and range from 1,000°C to 1,500°C. The compositions of both alloys are given in Table 3. All of the graphical module default phases in Thermo-Calc are included.

Table 3 - Compositions for Phase Diagrams

Element:	Ni	Cr	Fe	Nb	Mo	Al	Ti	C
AM_MaxC Atomic Percent	45.73-25.73	21.86	19.07	0-20	1.92	1.26	1.24	0.3838
Ni-Cr-Fe-Nb Atomic Percent	59.07-39.07	21.86	19.07	0-20	0	0	0	0

2.1.2.3 Scheil Diagram

Two Scheil Diagrams are calculated using Thermo-Calc. One diagram shows the Scheil solidification path for the AM samples assuming no carbon content (AM_NoC). The other phase diagram shows the Scheil solidification path for the AM samples assuming the hypothetical maximum carbon content (AM_MaxC). The simulations start at 1,400°C and terminate once Thermo-Calc determines ~100% of the liquid has transformed to solid. The compositions of both alloys are given in Table 4. All of the graphical module default phases in Thermo-Calc are included.

Table 4 - Compositions for Scheil Diagrams

Element:	Ni	Cr	Fe	Nb	Mo	Al	Ti	C
AM_NoC Atomic Percent	51.4	21.86	19.07	3.25	1.92	1.26	1.24	0
AM_MaxC Atomic Percent	51.0162	21.86	19.07	3.25	1.92	1.26	1.24	0.3838
AM_NoC Weight Percent	51.85	19.68	18.44	5.23	3.19	0.59	1.03	0
AM_MaxC Weight Percent	51.8	19.66	18.42	5.22	3.19	0.59	1.03	0.080

2.1.2.4 Step Diagram

Four step diagrams are calculated by Thermo-Calc. The step diagrams are essentially the calculation of phase fractions and phase compositions based on the phase diagrams for one alloy composition. The four step diagrams calculated are for the following compositions:

1. The cast sample composition, assuming no carbon (AC_NoC);

2. The cast sample composition, assuming the hypothetical maximum carbon content (AC_MaxC);

3. The AM sample composition, assuming no carbon (AM_NoC);

4. The AM sample composition, assuming the hypothetical maximum carbon content (AM_MaxC).

The simulations range in temperature from 500°C to 1,180°C. The compositions of all four alloys are given in Table 5. All of the graphical module default phases in Thermo-Calc are included.

Table 5 - Compositions for Step Diagrams

Element:	Ni	Cr	Fe	Nb	Mo	Al	Ti	C
AC_NoC Atomic Percent	51.89	20.85	19.36	3.44	1.94	1.19	1.33	0
AC_MaxC Atomic Percent	51.5062	21.86	19.07	3.25	1.92	1.26	1.24	0.3838
AM_NoC Atomic Percent	51.4	21.86	19.07	3.25	1.92	1.26	1.24	0
AM_MaxC Atomic Percent	51.0162	21.86	19.07	3.25	1.92	1.26	1.24	0.3838
AC_NoC Weight Percent	52.40	18.65	18.60	5.50	3.20	0.55	1.10	0
AC_MaxC Weight Percent	52.36	18.64	18.59	5.49	3.20	0.55	1.09	0.08
AM_NoC Weight Percent	51.85	19.68	18.44	5.23	3.19	0.59	1.03	0
AM_MaxC Weight Percent	51.8	19.66	18.42	5.22	3.19	0.59	1.03	0.080

2.1.2.5 Diffusion Simulation

Four diffusion simulations are calculated by the DICTRA module of Thermo-Calc. The diffusion simulations are based on EDS scans across γ matrix and Laves phase in both as-cast and as-built samples. The results of the EDS scans are provided in Appendix B. The EDS scan compositions are included in DICTRA via Heaviside functions. The four analyses run are

1. The as-cast sample EDS scan composition, assuming no carbon;

2. The as-cast sample EDS scan composition, assuming no carbon, but with all minor element (Mo, Al, Ti) converted to Ni;

3. The as-built sample EDS scan composition, assuming no carbon;

4. The as-built sample EDS scan composition, assuming no carbon, but with all minor element (Mo, Al, Ti) converted to Ni.

The simulations are conducted at a temperature of 1,180°C. Only the disordered FCC phase (γ) is included in the analysis.

2.2 Experiments

Inconel 718 rod samples with a diameter of 15 mm and a length of 40 mm were made by suction casting under an Argon atmosphere using an ABJ-338 arc-melter (Materials Research Furnaces Inc.). AM Inconel 718 samples were built by PBF using an EOS M 290 machine with the default processing parameters for Inconel 718 alloy. The nominal compositions of the cast alloy and powders of Inconel 718 are listed in Table 5. Both as-cast and as-built samples were denoted as AC and AM respectively, sectioned into smaller parts, and encapsulated into vacuumed quartz tubes back-filled with pure Argon gas. In total there were four cast samples and four AM samples to allow for various heat treatment times. Afterwards, both cast and AM samples were homogenized at 1,180°C for 20 minutes, 1 hour, or 12 hours followed by quenching in ice-water. Sample notations with homogenization conditions are shown in Table 6.

Following the heat treatment, all eight samples were surface polished using the standard procedures. After surface polishing, microstructures of both as-received (as-cast and as-built) and as-homogenized samples were characterized and analyzed by electron microscopes. SEM (Zeiss Sigma 500 VP, Carl Zeiss AG) and EDS (Oxford Instruments plc) characterizations were carried out for phase morphology observation and composition determination. EBSD (FEI Scios

DualBeam, FEI Company) was employed to investigate the recrystallization behaviors of the homogenized samples with a mapping area of 1,200 μm × 1,200 μm and step size of 1.6 μm for each sample. The EBSD results were analyzed by OIM Analysis™ v8 software package.

3.0 Results

3.1 Computational Results

3.1.1 Temperature Transient

The calculated density of the Inconel 718 sample at 1,180°C is 7.82 g/cm³. The GFE of the sample is calculated via Thermo-Calc and shown in Figure 1 along with the derivative of the GFE with respect to temperature at constant pressure, with spikes in the data removed. The blue line corresponds to the left axis, and the orange line corresponds to the right axis. The calculated specific heat capacity is shown in Figure 2, with spikes in the data removed. The calculated specific heat capacity includes all equilibrium phase transitions, even though not all of the equilibrium phase transitions are present in the samples. The calculated radiative heat flow versus time is shown in Figure 3. The heat flow is large while the difference in temperature is large, but the heat flow reduces as the sample approaches the target temperature due to the radiative heat transfer being a function of $T_f^4 - T_s^4$. The temperature transient of the sample is shown in Figure 4, with the temperature of the furnace and the temperature of the sample plotted versus time. The temperature transient of the sample is shown in Figure 5, with the sample's percent of target temperature plotted versus time. The blue line corresponds to the right axis, and the orange line corresponds to the left axis. Both lines are the same data, but on different scales. The percent of target temperature is calculated based on absolute temperatures. The sample reaches 98% of the target temperature within three minutes, and 99.5% within four minutes.
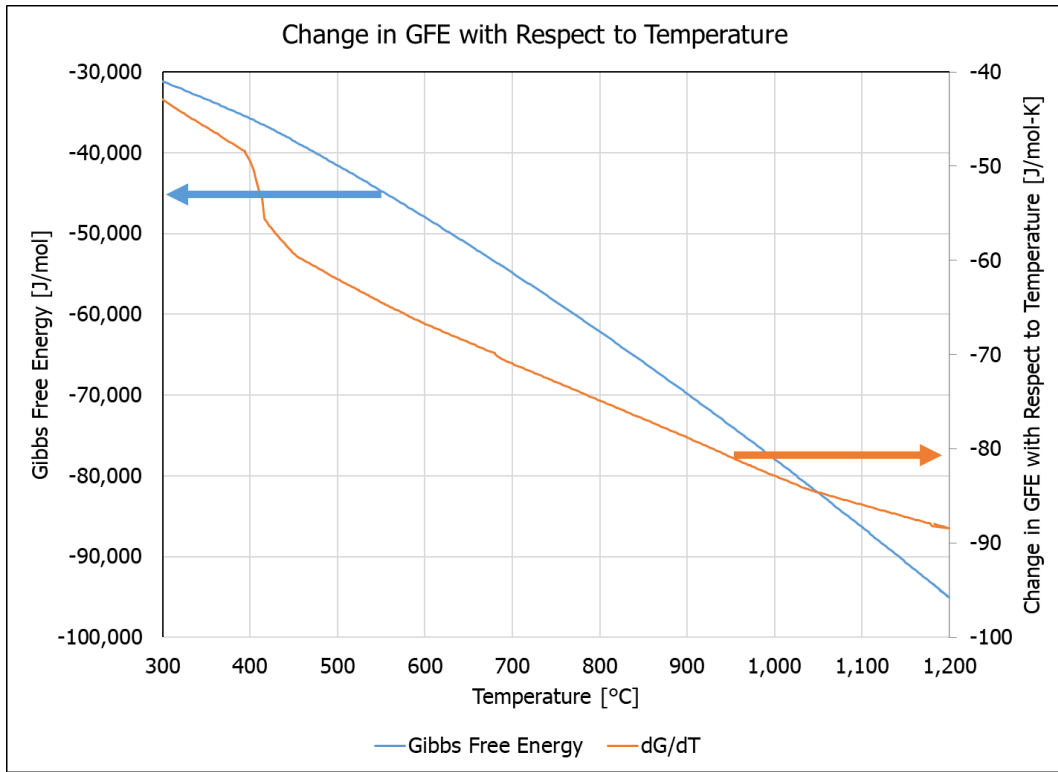
Figure 1 - Gibbs Free Engery and dG/dT of Inconel 718 vs. Temperature at Constant Pressure
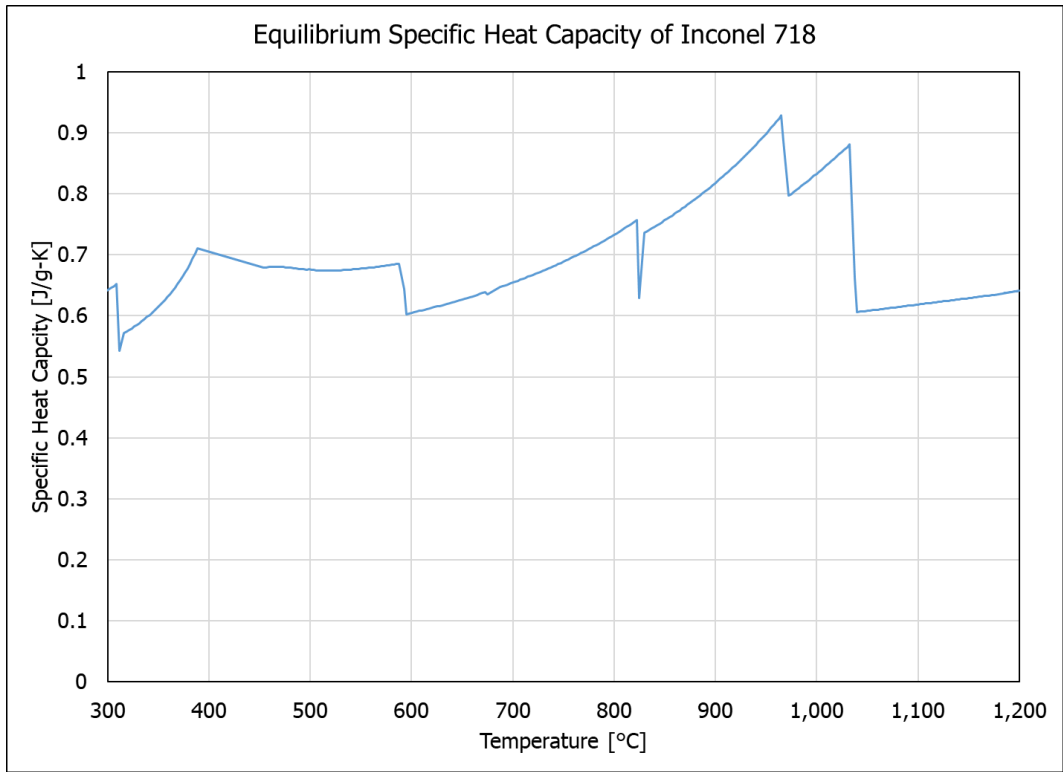
Figure 2 - Specific Heat Capcity of Inconel 718 versus Temperature
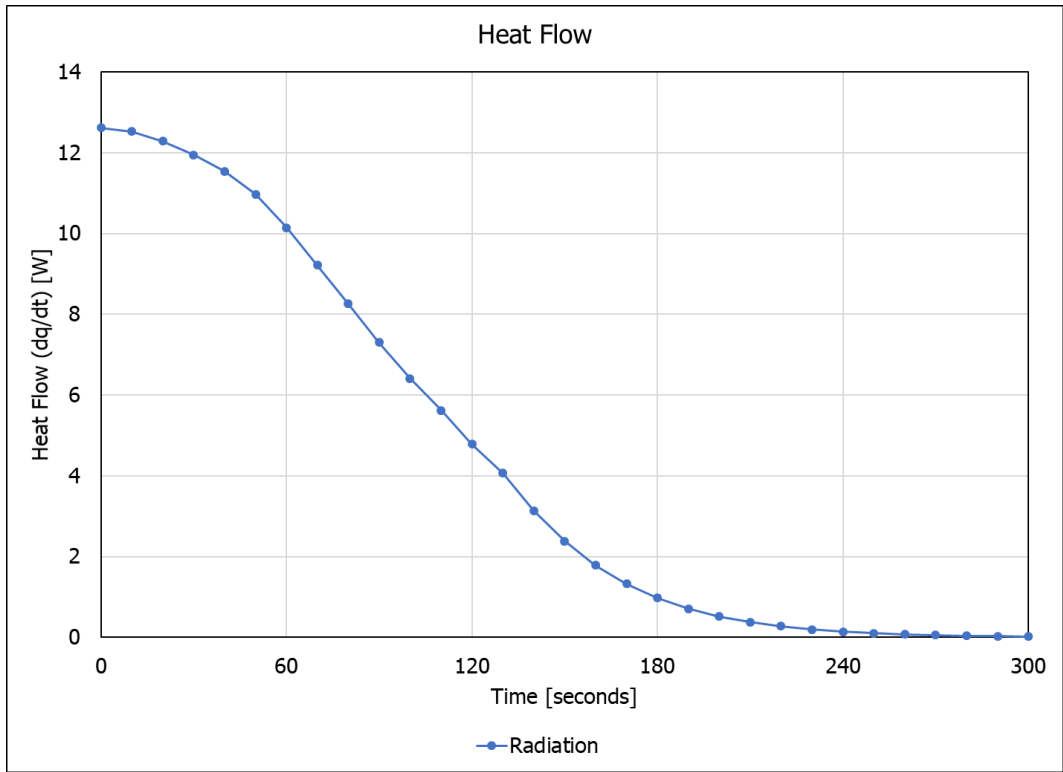
Figure 3 - Radiative Heat Flow in Sample
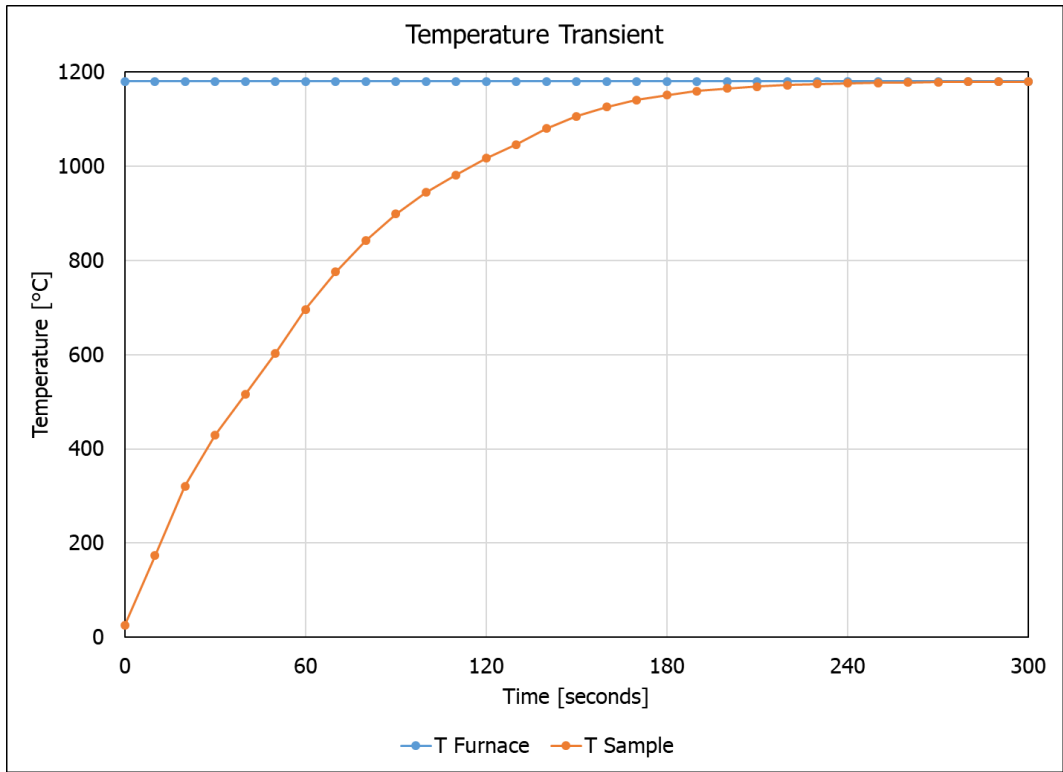
Figure 4 - Temperature Transient of Sample
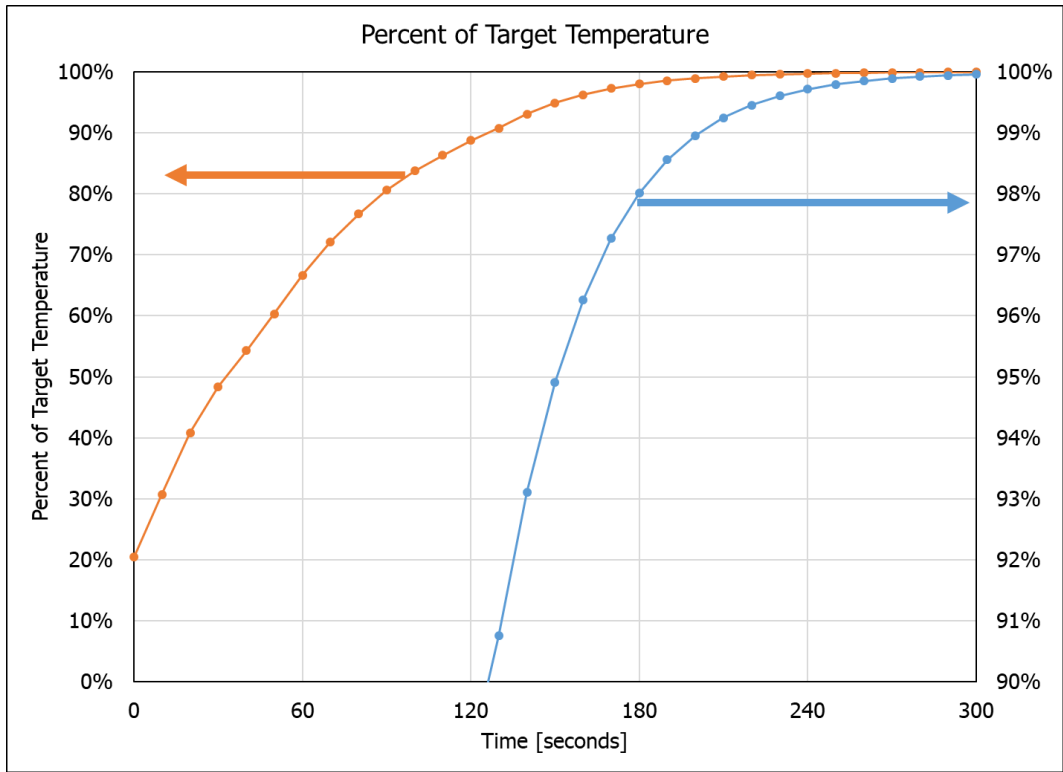
Figure 5 - Temperature Transient as Percent of Target Temperature

3.1.2 Phase Diagram

The calculated phase diagram for the AM alloy with assumed maximum carbon content is shown in Figure 6. Select phases are labeled. The composition plotted varies in Ni and Nb content. The AM sample has an average Nb content of 3.25 atomic percent. Due to the complexity of the 8-component phase diagram, a simplified 4-component phase diagram is shown in Figure 7. The alloy has 21.86 atomic percent Cr, 19.07 atomic percent Fe, and the balance is Ni and Nb. Select regions are labeled. Special attention should be paid to the variable γ Nb content on solidification, and that if the local Nb concentration is above ~7%, then Laves phase becomes an equilibrium phase. The composition plotted varies in Ni and Nb content. Similarities between the two phase diagrams can be seen, especially by looking at the γ+Liquid-Liquid interface, and the Laves+Liquid-Liquid interface.
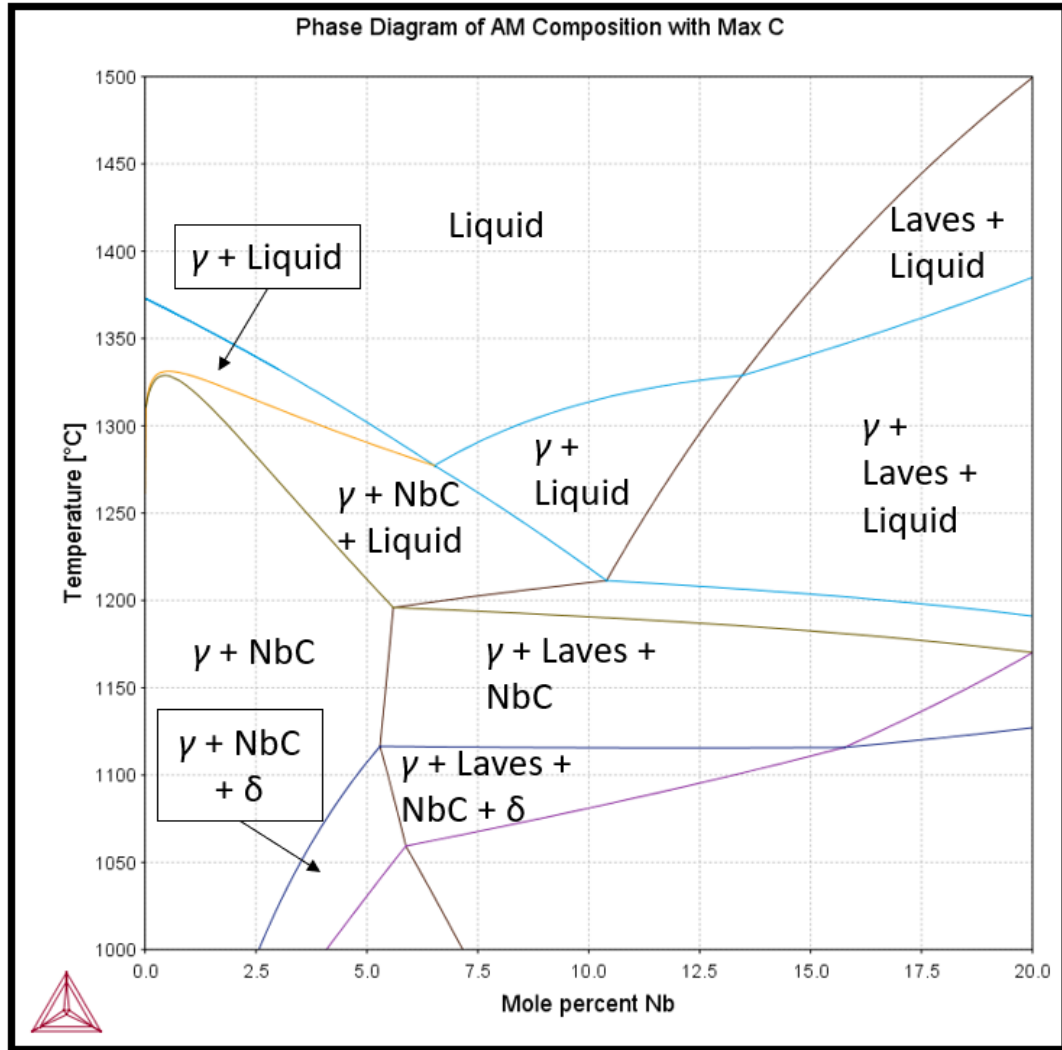
Figure 6 - Phase Diagram of AM Composition with Maximum Carbon Content
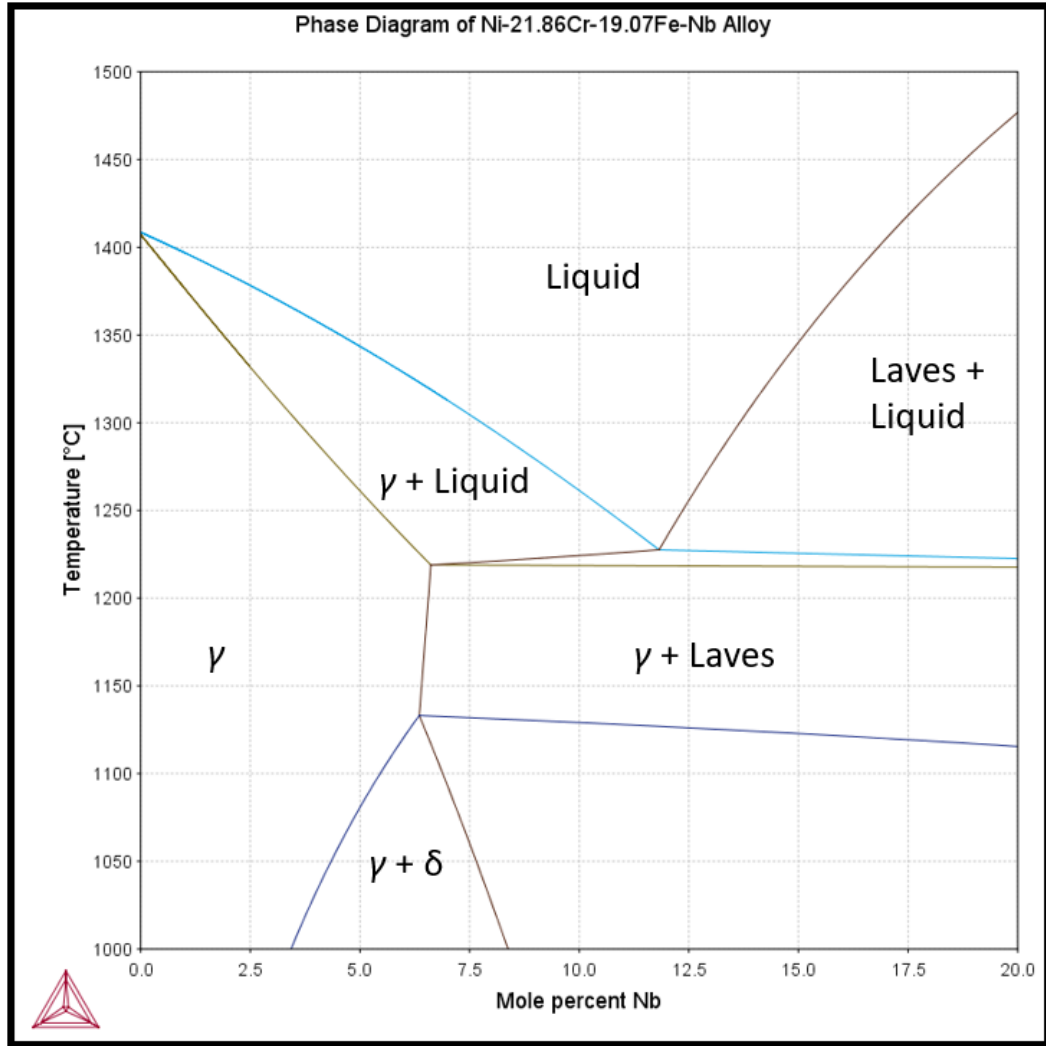
Figure 7 - Phase Diagram for Simplified Alloy

3.1.3 Scheil Diagram

The result of the Scheil calculation for the AM composition with no carbon is shown in Figure 8. The dashed line shows equilibrium cooling. The color of the line changes as phases are added. In order to show the effect of carbon content on the solidification behavior, the result of the Scheil calculation for the AM composition with maximum carbon is shown in Figure 9. The dashed line shows equilibrium cooling. The color of the line changes as phases are added.
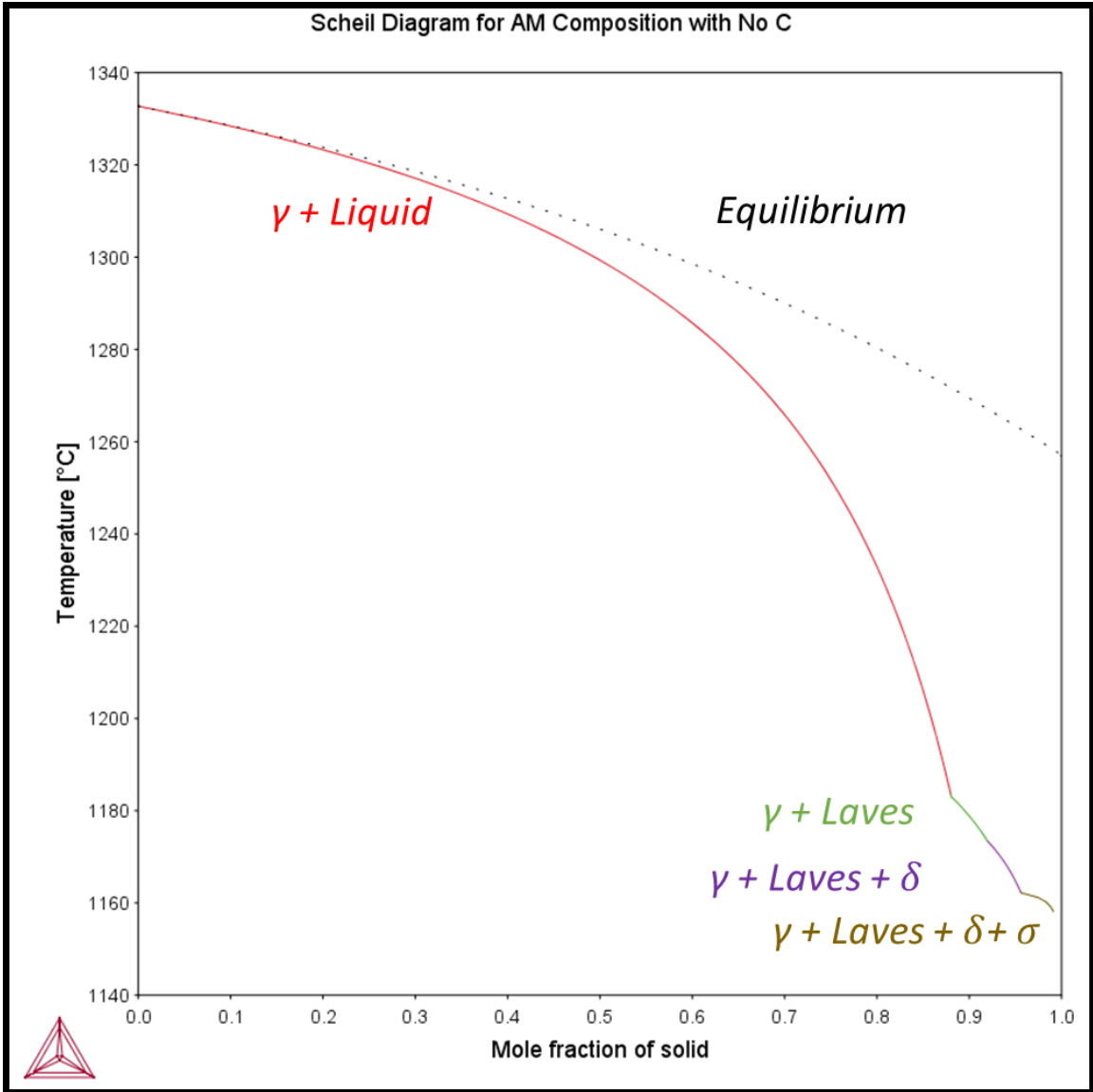
Figure 8 - Scheil Diagram for AM Composition with No Carbon
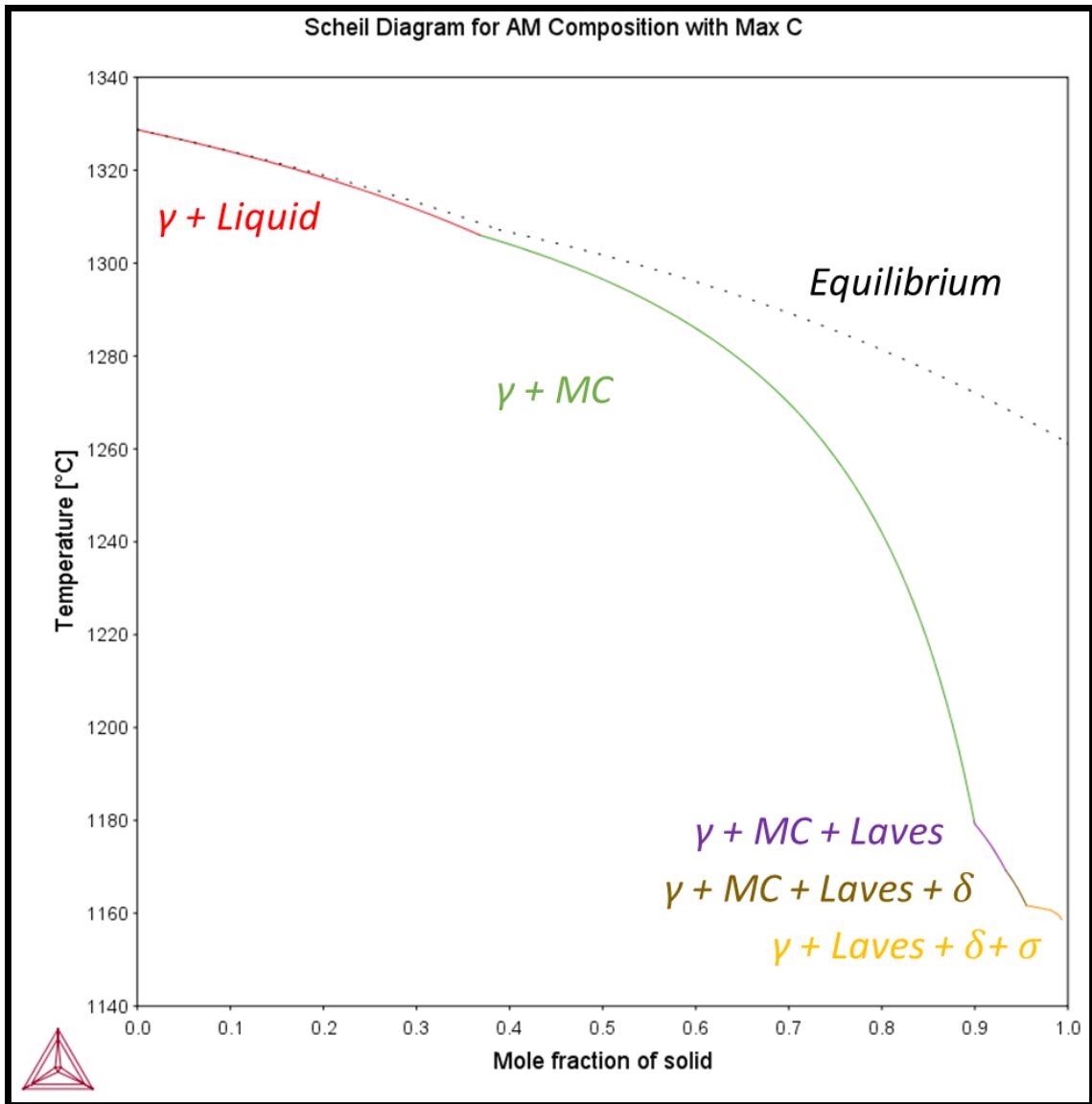
Figure 9 - Scheil Diagram for AM Composition with Maximum Carbon

3.1.4 Step Diagram

The step diagram for the AC composition with no carbon is shown in Figure 10. To quantify the effect of adding carbon, the step diagram for the AC composition with maximum carbon is shown in Figure 11. The phase fractions add up to 1.0. The Y-axis is in a log-scale. Different colors are different solid phases. The equilibrium phase fraction of MC carbide is approximately 0.8%. To compare the different equilibrium phase fractions between AC and AM samples, the same step diagrams are created for the AM composition with no carbon and maximum carbon in Figure 12 and Figure 13, respectively. The equilibrium phase fraction of MC carbide is approximately 0.8%.
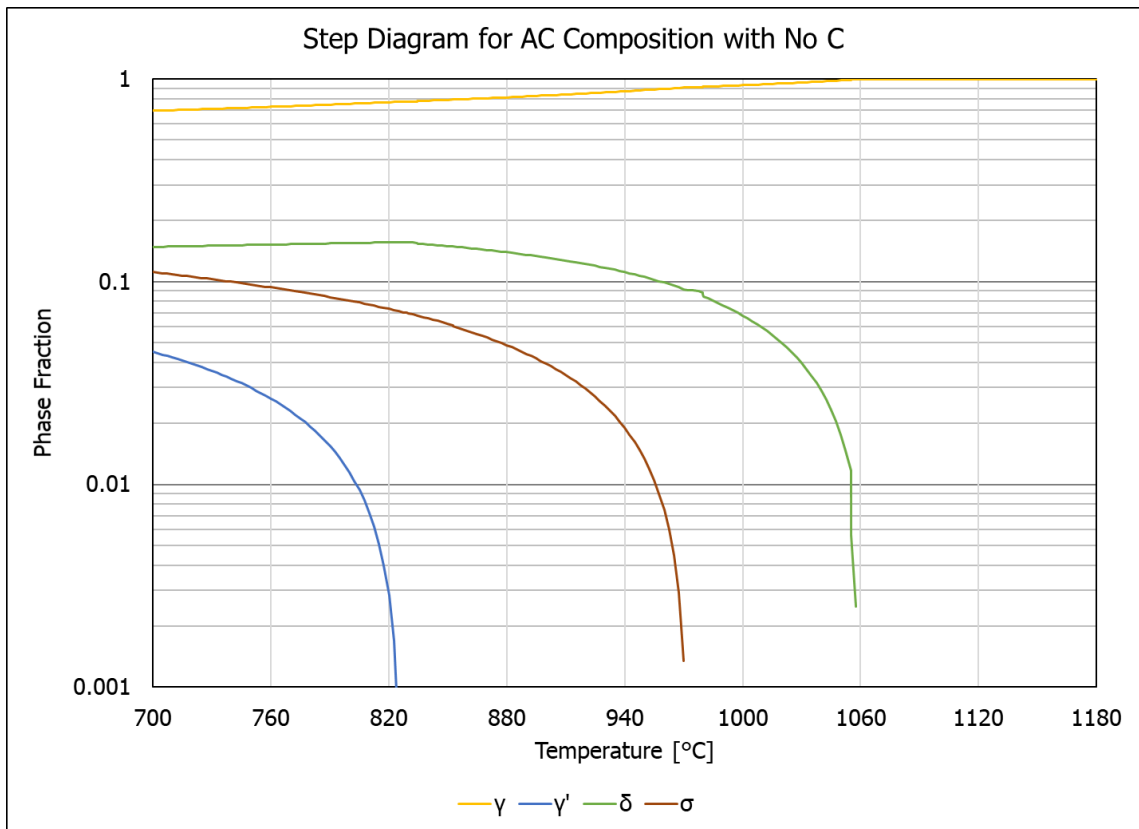
Figure 10 - Step Diagram for AC Composition with No Carbon
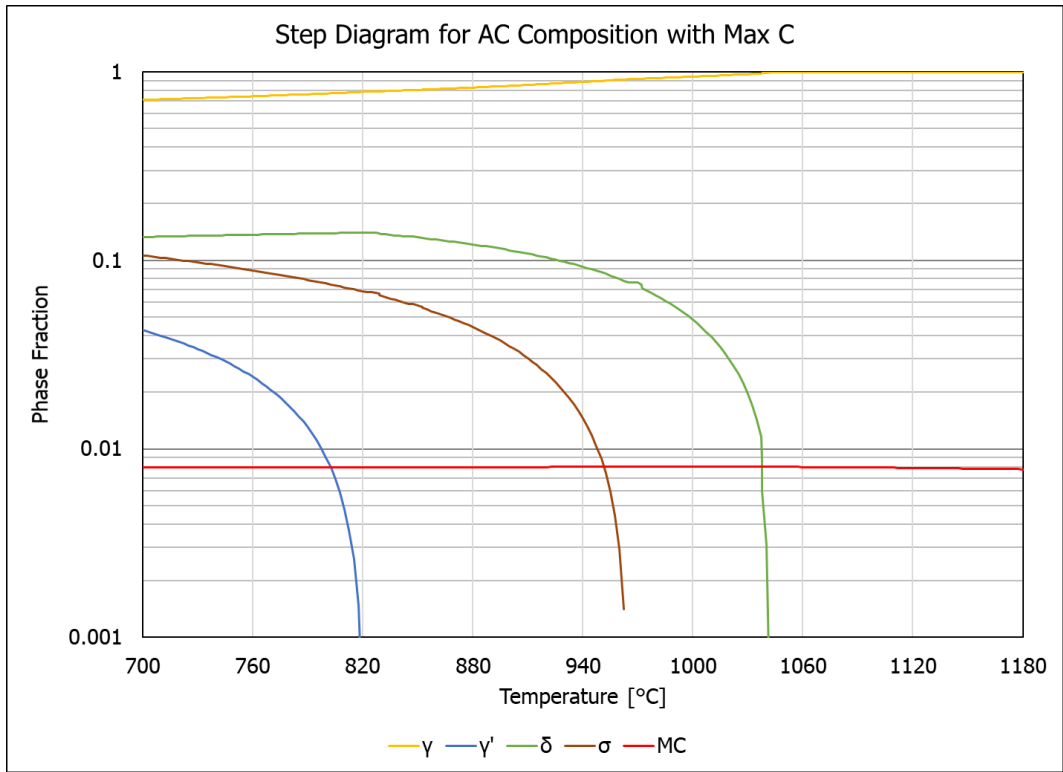
Figure 11 - Step Diagram for AC Composition with Maximum Carbon
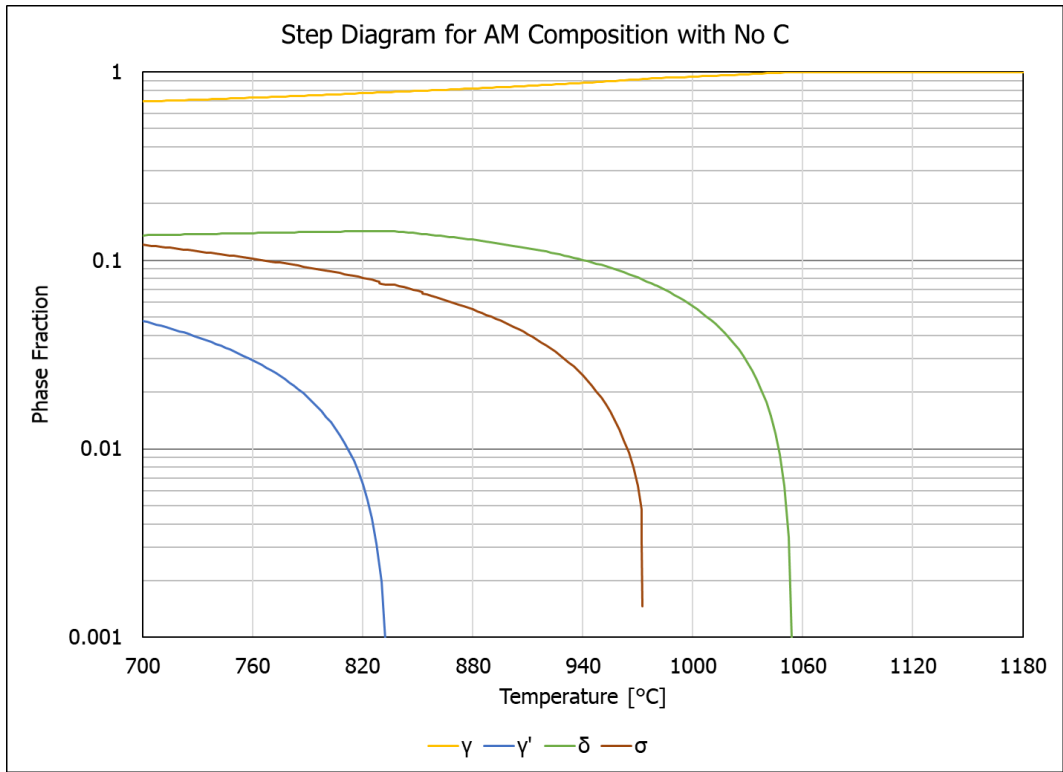
Figure 12 - Step Diagram for AM Composition with No Carbon
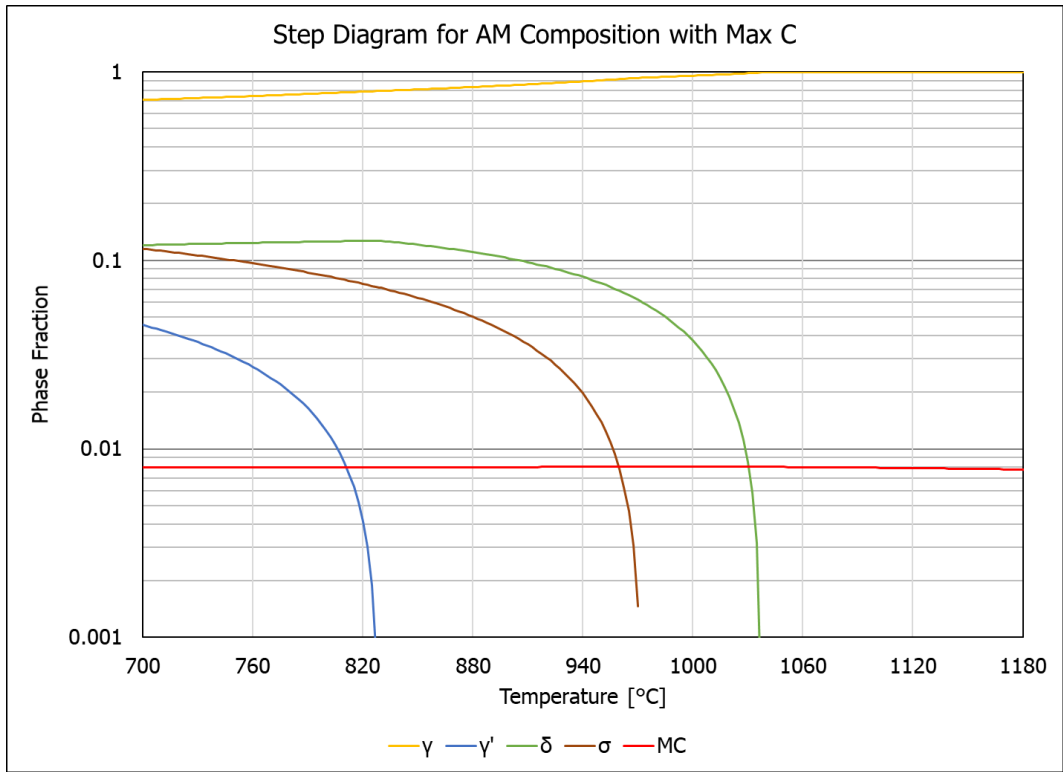
Figure 13 - Step Diagram for AM Composition with Maximum Carbon

3.1.5 Diffusion Simulations

The DICTRA diffusion result for the cast sample is shown in Figure 14; the full elemental composition from the EDS scan is used. Each line is the spatial distribution of the Nb for a different length of homogenization heat treatment: 0 is for 0 seconds of heat treatment; 0.036 is for 0.036 seconds of heat treatment, etc. All of the material is assumed to be disordered γ matrix phase. The elemental composition is based on EDS scan results in Table 7. The diffusion result for the cast sample with a reduced element set without Ni-Cr-Fe-Nb content is shown in Figure 15; all of the minor elements from the EDS scan are converted into Ni for this simulation to see the effect of simplifying the alloy. The diffusion result for the AM sample is shown in Figure 16; the full elemental composition from the EDS scan is used. Each line is the spatial distribution of the Nb for a different length of homogenization heat treatment: 0 is for 0 seconds of heat treatment; 0.036 is for 0.036 seconds of heat treatment, etc. All of the material is assumed to be disordered γ matrix phase. The elemental composition is based on EDS scan results in Table 8. Because the reduced element set result is very similar to the full element set results, the reduced element result for the AM sample is not presented. The four diffusion simulations results are distilled into one plot in Figure 17 that shows the average Nb content from the EDS scan divided by the maximum Nb content at any point within the simulation. 100% indicates that the average Nb content is equal to the maximum Nb content and the sample is fully homogenized. For reference, 20 minutes and 1 hour are included in the plot.
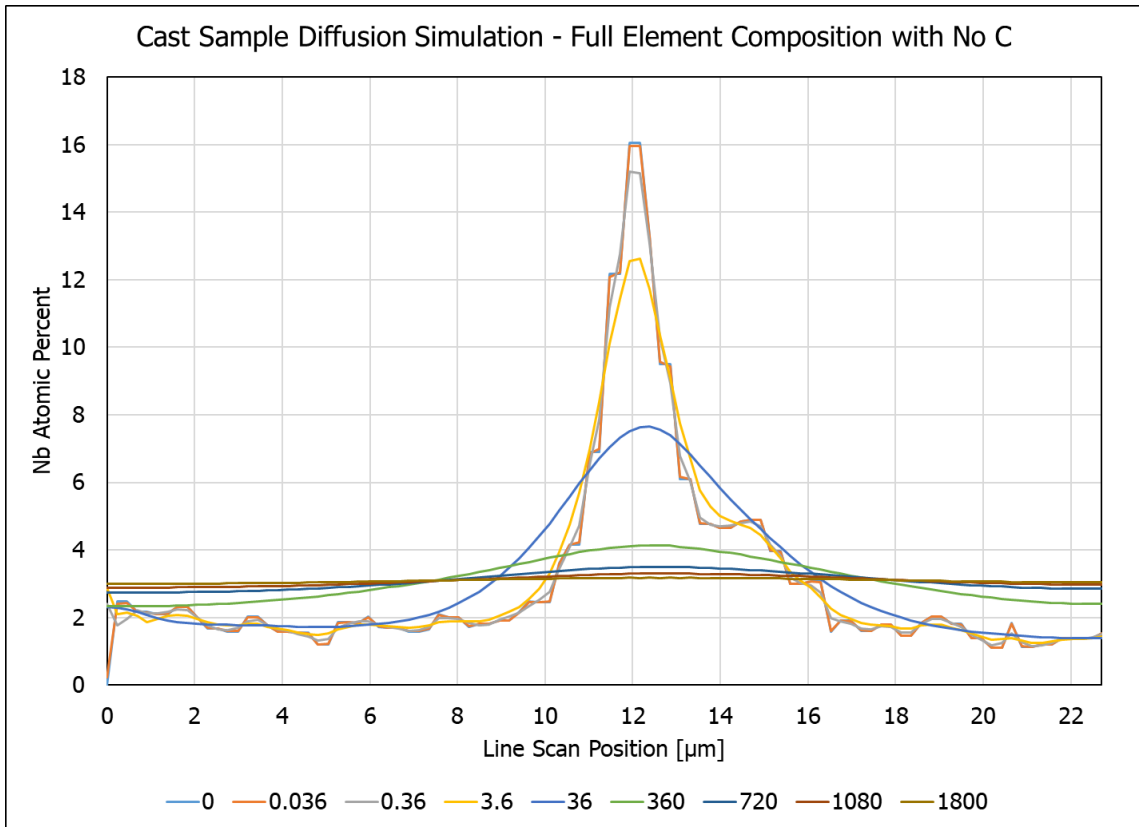
Figure 14 - DICTRA - Cast Sample - Full Elemental Set - No C
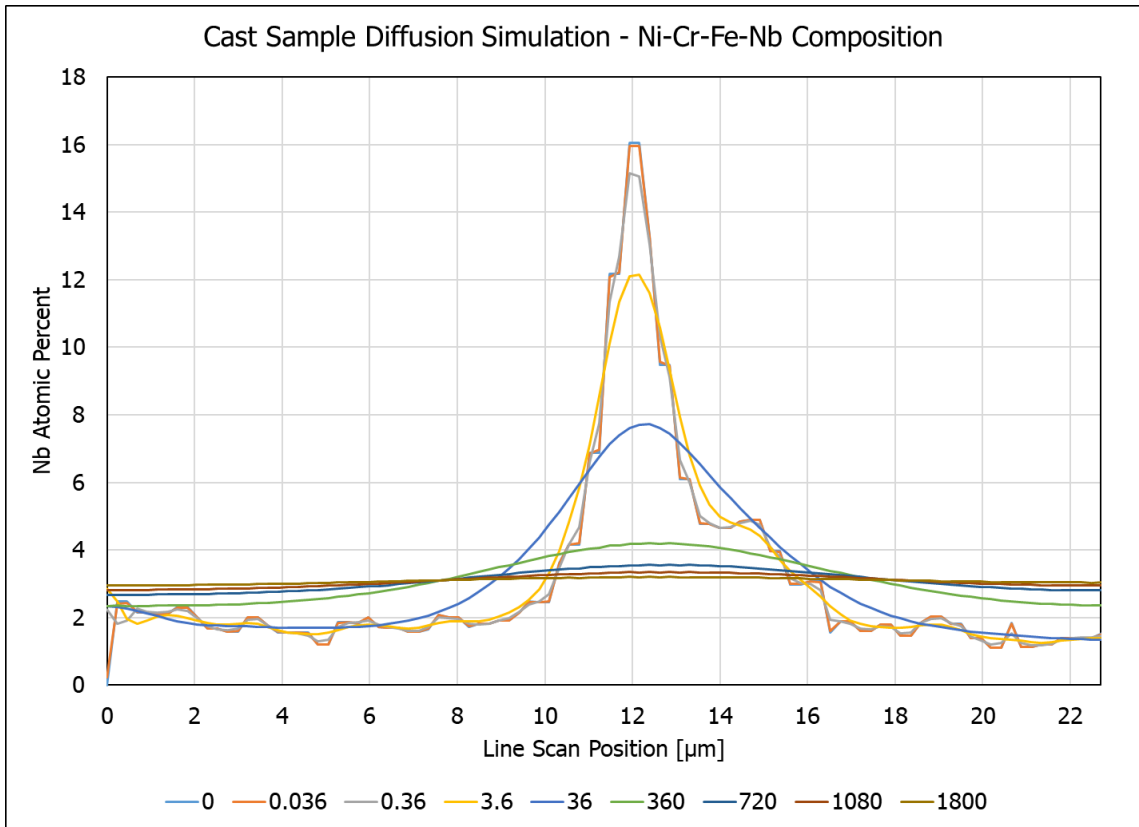
Figure 15 - DICTRA - Cast Sample - Reduced Element Set - No C
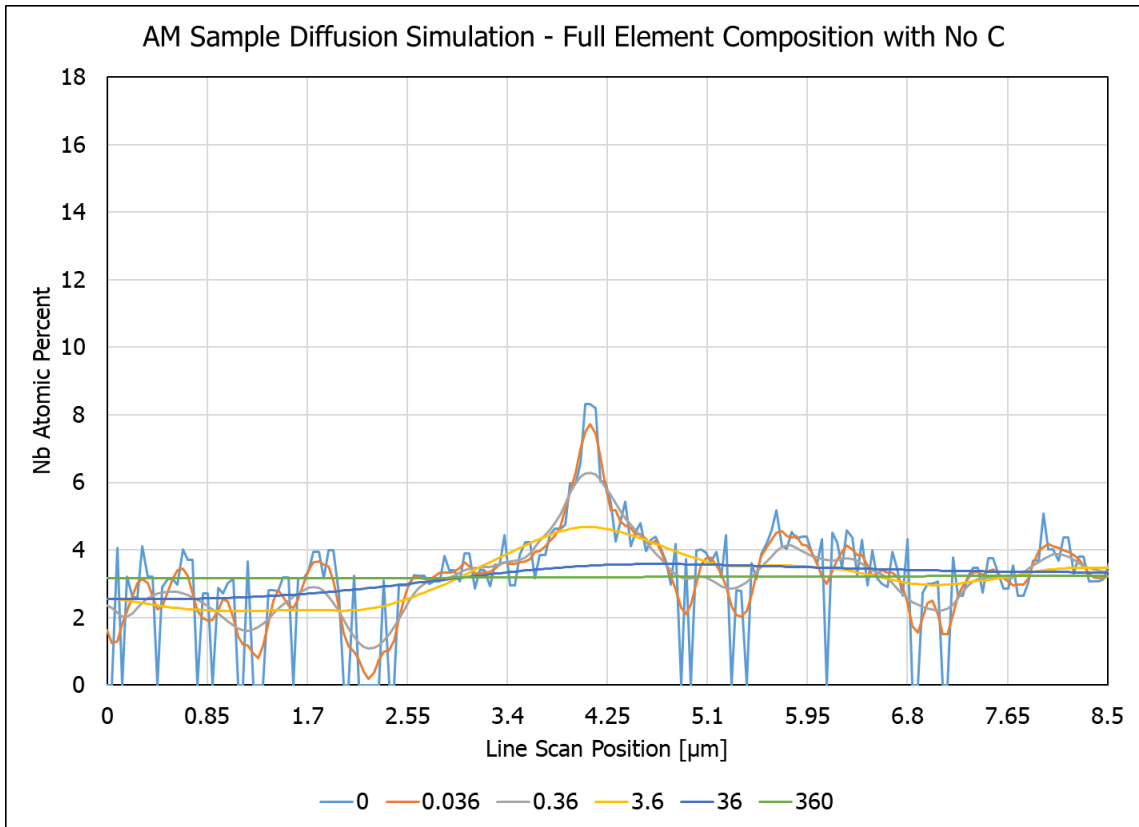
Figure 16 - DICTRA - AM Sample - Full Elemental Set - No C
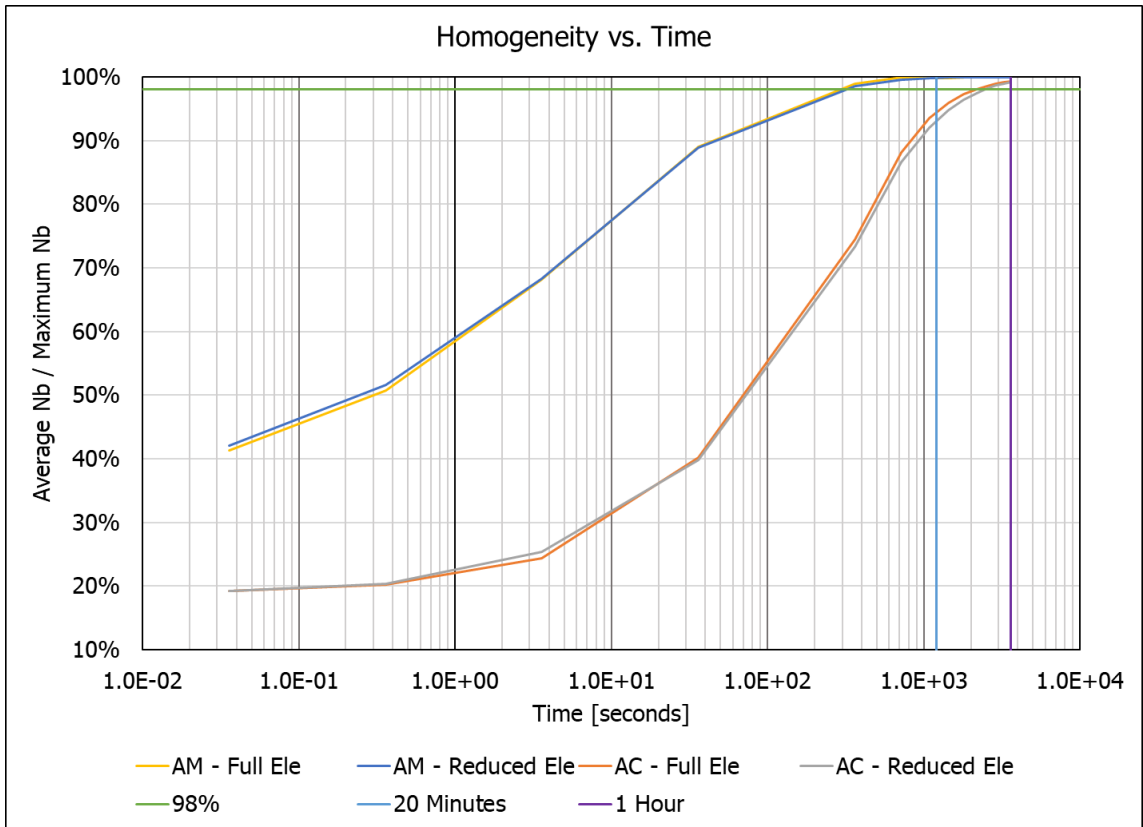
Figure 17 - Combined DICTRA Results.

3.2 Experiments

The results of the eight SEM experiments are shown in Figure 18. The top four images are for the cast sample, and the bottom four images are for the AM sample. The leftmost images are the as-received (non-heat-treated) samples, and heat treatment length increases towards the right. Because backscatter electrons are used for the imaging, high atomic number atoms will reflect more electrons and show up as brighter portions in the image. Nb and Mo are the heaviest elements in the samples and thus Nb and Mo segregation, which is in MC and Laves phases, can be measured via SEM. The results of the image analysis of Figure 18 are given in Table 6. All images are taken from the same plane, with the build direction in the plane, as demonstrated by the melting pool lines in Figure 18(e).
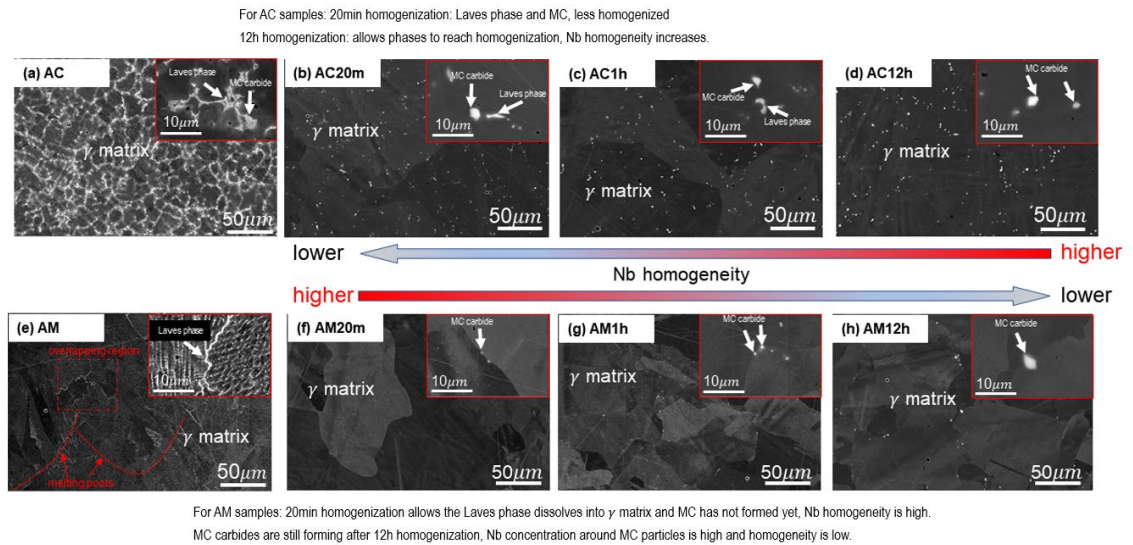
Figure 18 - SEM Characterized Microstructure of Samples

Table 6 - SEM Image Analysis Results

	Homogenization time:	20min	1h	12h
MC (+Laves phase) fraction:	AM	~0	0.05%	0.36%
	AC	0.73%	0.65%	0.47%

Prior to heat treatment, EDS scans were performed across representative Laves interdendritic regions. The results of the EDS scans are shown in Figure 19, with the cast sample on the left and the AM sample on the right. The SEM image used for guiding the EDS scan is shown above the EDS plot. The tabulated results of the EDS scan for all elements are provided in Table 7 for the cast sample and in Table 8 for the AM sample. No carbon content is listed because EDS cannot find light elements.
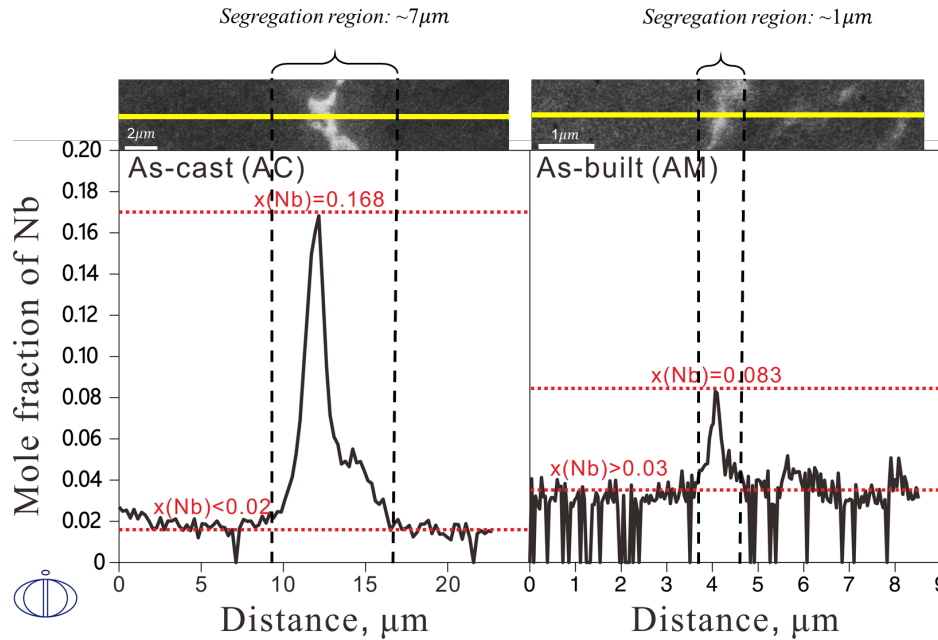
Figure 19 - EDS Line Scanning across Laves Phase in Cast and AM samples

In order to measure the Nb distribution around MC carbides, an EDS map is made for each of the six heat treated samples. To make the map, a MC carbide without neighboring MC carbides is located and a 5 x 5 grid of EDS scans is made with the MC carbide at the center of the grid, as shown in Figure 20. Three such scans are made and averaged for each plot in Figure 21. To plot the results, the middle point (with the MC carbide) is removed to avoid skewing the results with the roughly 50% Nb content. The results are shown as a heat map in Figure 21 with black lines denoting where the MC carbide is located. The AC20m sample had neighboring MC carbides.
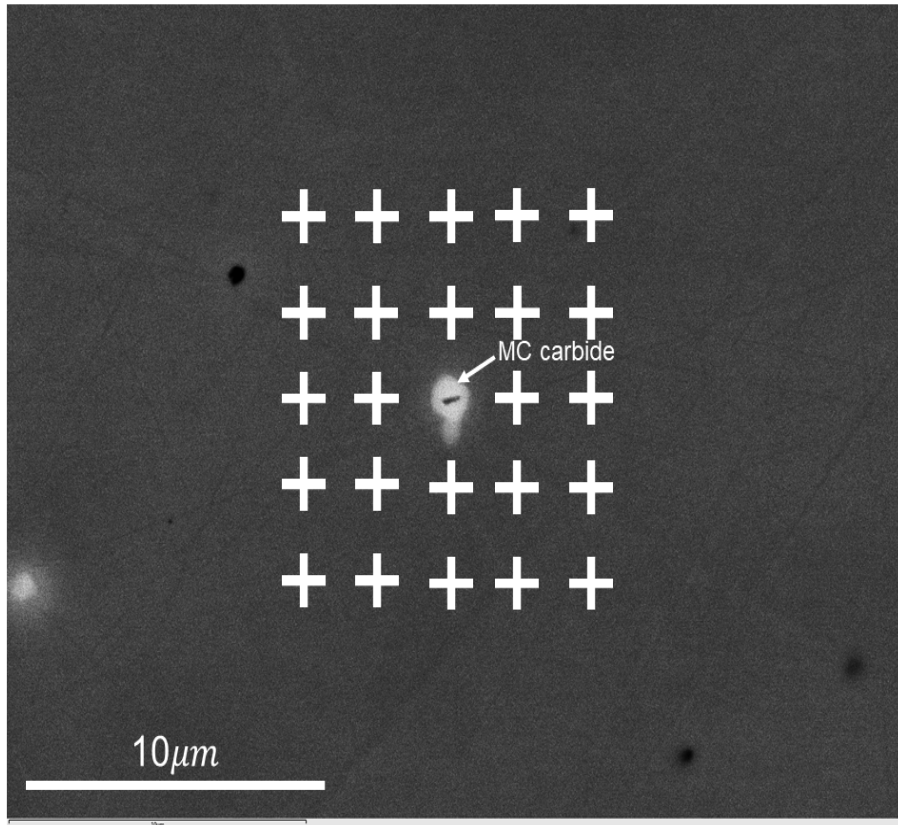
Figure 20 - EDS Mapping on Investigation of Nb Distribution, AC12 Sample as An Example
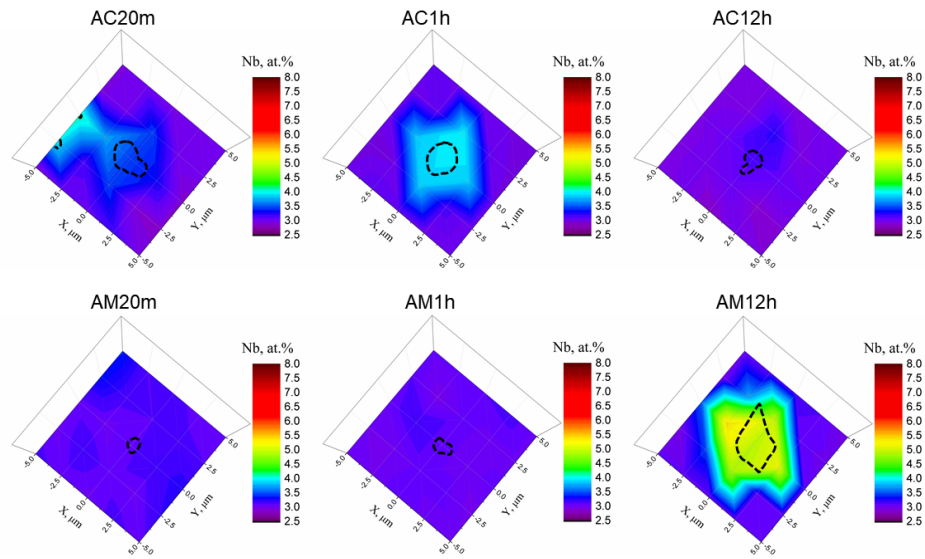
Figure 21 - EDS Mapping Results for Heat Treated Samples

The EBSD scan results for the eight samples are shown in Figure 22. The scan is shown in Inverse Pole Figure (IPF) mode, with the color corresponding to the grain orientation. Grains with a [001] orientation show as red, [101] show as green, and [111] show as blue. Only the FCC phase is included in the mapping algorithm. The average grain size from the images is presented in Figure 23 for the eight samples. The grain diameter distributions for the eight samples are shown in Figure 24, with the cast samples shown on the left and the AM samples shown on the right. The Grain Orientation Spread (GOS) for each of the eight samples is shown as a heat map in Figure 25 and plotted as a distribution in Figure 26.
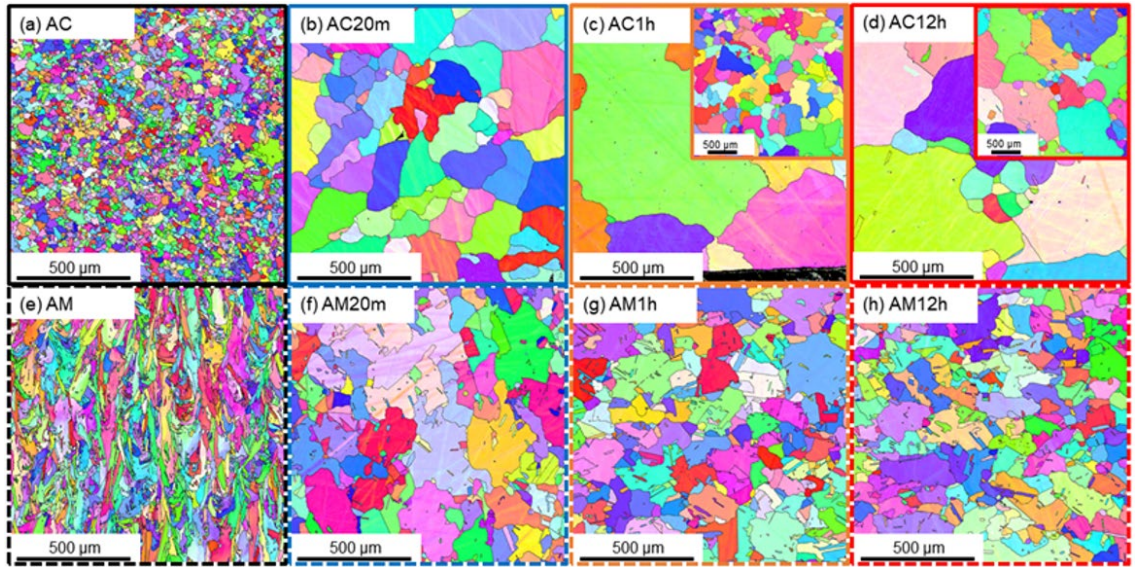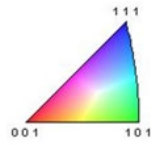
Figure 22 - Inverse Pole Figure of Samples from EBSD
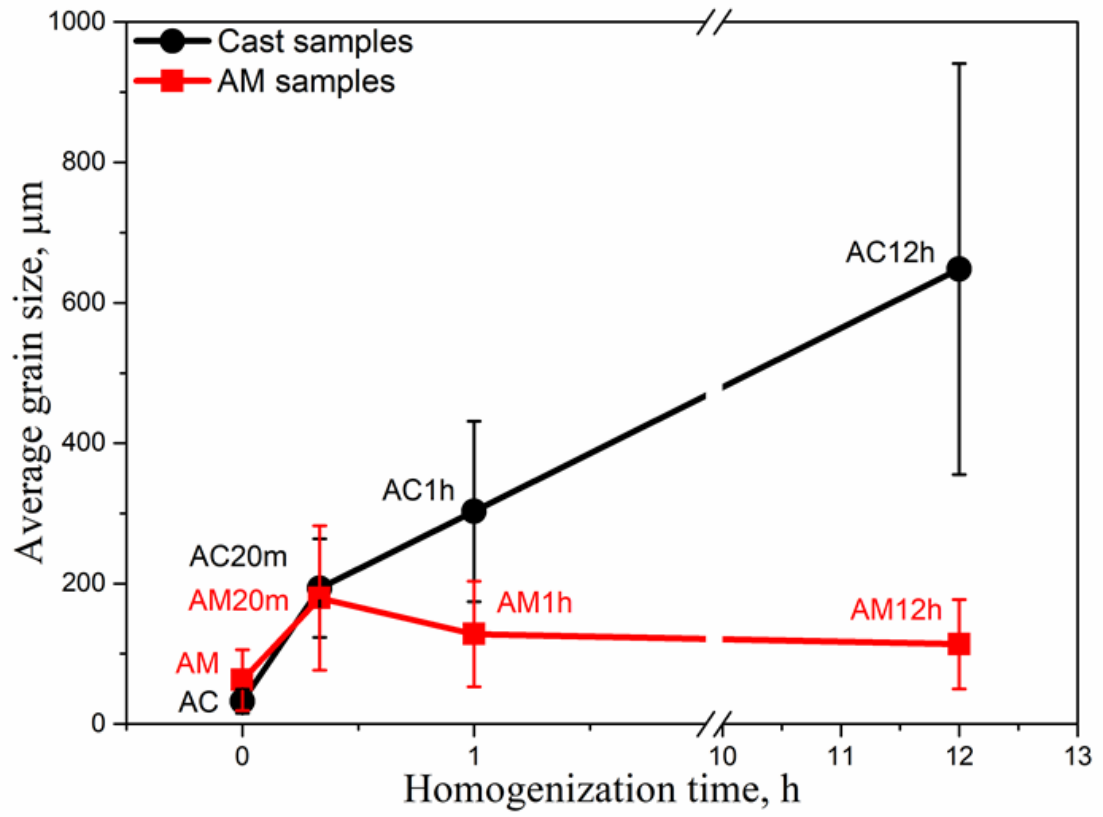
Figure 23 - Average Grain Size vs. Homogenization Time
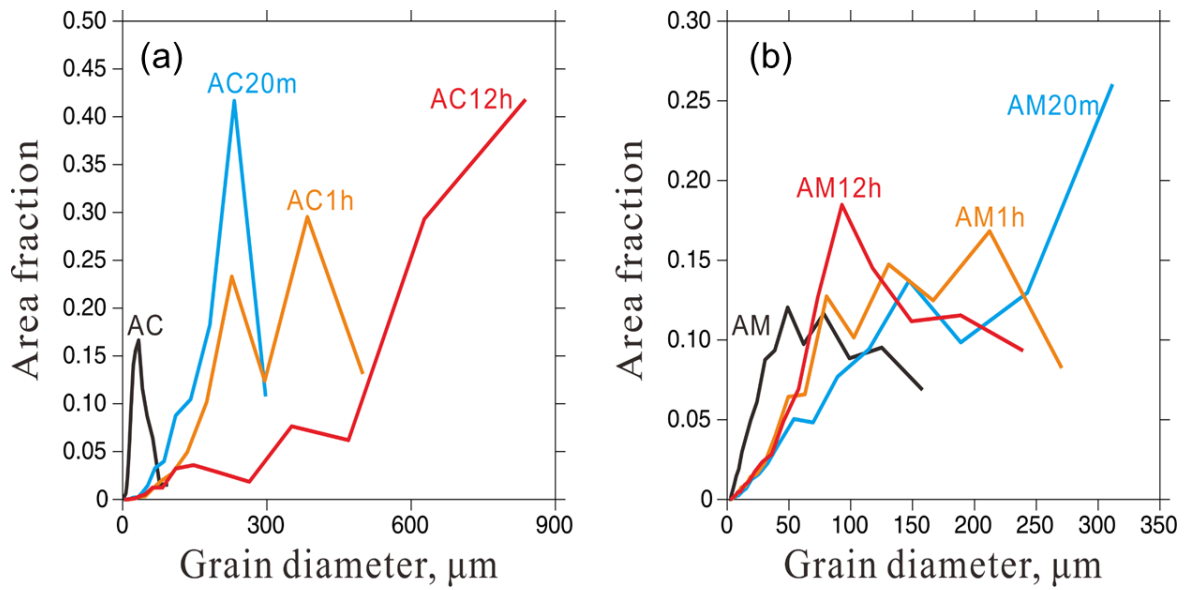
Figure 24 - (a) Grain Size Distribution - AC (b) Grain Size Distribution - AM
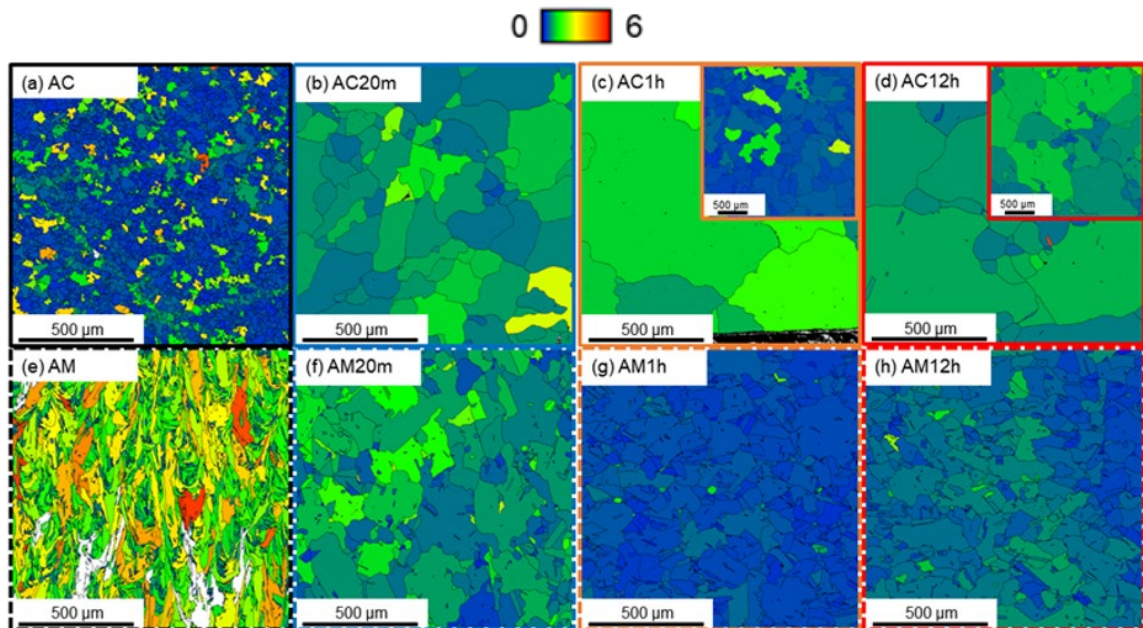
Figure 25 - Grain Orientation Spread Map of Samples from EBSD
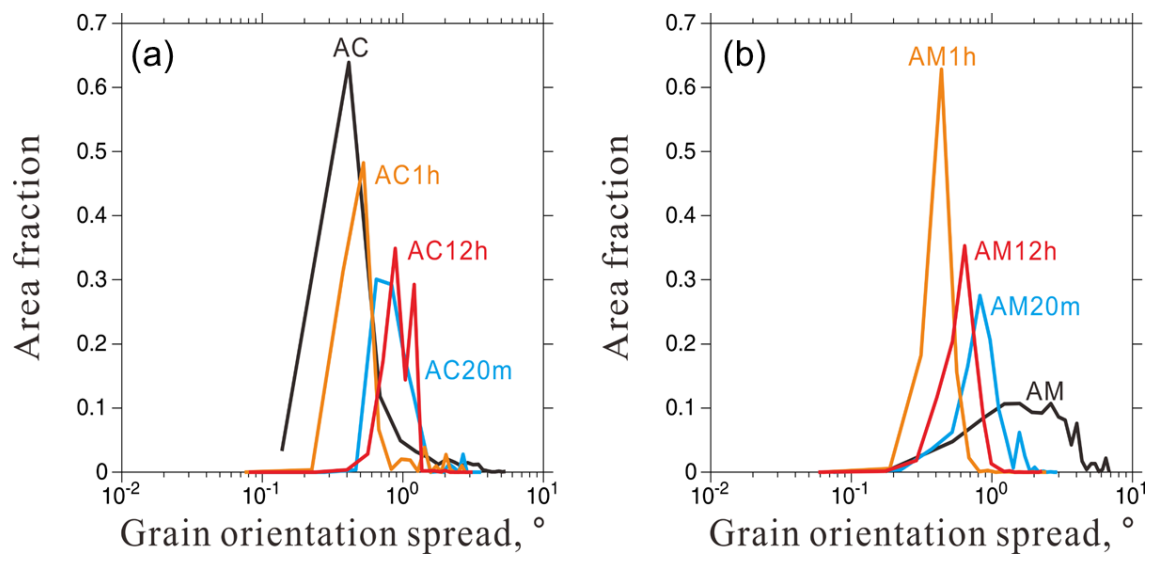
Figure 26 - (a) GOS - AC (b) GOS - AM

4.0 Discussion

4.1 Discussion of Calculations and Comparison to Experiments

In order to verify the accuracy of the homogenization heat treatment times listed (20 minutes, 1 hour, 12 hours), which are based on the amount of time the sample spent in the furnace, the calculation of the temperature transient was performed. The specific heat capacity shown in Figure 2 is based on the equilibrium phases in Inconel 718, which are not the phases present in the samples, as demonstrated by the Scheil calculation presented in Figure 9. However, as shown in Figure 9, the majority of the solid formed during solidification is γ and MC carbide, which corresponds to the dominant equilibrium solid phases shown in the step diagram in Figure 13 at 1,180°C and thus also corresponds to the right-most section of the specific heat diagram (Figure 2). As seen in Figure 2, the right-most portion from ~1,050°C to 1,180°C, which corresponds to γ and MC carbide phases, has a lower than average specific heat, thus it is conservative to use the calculated equilibrium specific heat values for the transient calculation because it will overestimate the time required to heat the sample. From Figure 5 it is seen that the sample reaches 98% of the target temperature within 3 minutes, and 99.5% of the target temperature within 4 minutes; this means that only about 3 minutes of the heat treatment are spent at temperatures significantly below the heat treatment temperature, which is a small amount compared to the heat treatment times. Based on the results of the temperature transient analysis, it is concluded that it is a reasonable approximation to base the heat treatment times on the total time spent in the furnace and ignore the heat up time. However, because this analysis shows that the very small sample (5 mm x 5 mm x 10 mm) heats up in 3-4 minutes, that indicates that larger samples, or samples where the surface

52

is shielded from radiative heating due to its complex geometry, which will take longer to heat up, may not be able to ignore the heat up time for heat treatments. AM parts with very complex internal geometries will have restricted heat conduction paths and the internal sections will heat up more slowly, thus resulting in a gradient heat treatment unless the experimentalist or manufacturer takes care to avoid under-heating the sample.

The phase diagrams in Figure 6 and Figure 7 give a better understanding of the solidification microstructure to expect and demonstrate that segregation should be expected. The slope of the solidus and liquidus of the γ+Liquid region in Figure 7 indicate that severe Nb segregation should be expected upon solidification; for the hypothetical alloy, as the first γ begins to form at ~1,360°, the Nb content in the γ is less than 2%, while the Nb content in the liquid is 3.44%. As further solidification occurs, the lack of Nb in the γ requires that there is more Nb in the liquid, which pushes the average Nb content to the right and eventually the liquid will undergo a eutectic reaction to produce γ and Laves. Comparing Figure 7 and Figure 6 shows that a similar process should be expected for the actual Inconel 718 alloy, but that there will additionally be MC carbides that contain a high percent of Nb. It is also shown that the actual Inconel 718 alloy will form solid at a lower starting temperature than the hypothetical alloy plotted in Figure 7, and that the Laves phase will form at lower Nb concentrations. Use of the phase diagrams in Figure 6 and Figure 7 in combination with the Scheil diagrams in Figure 8 and Figure 9 guides the expectations of the experiments.

Because it is known that the EDS used for determining the composition of the samples cannot determine the carbon content of the alloys, simulations are performed for both minimum and maximum carbon to estimate the range of values to be expected from the actual alloy. Figure 8 and Figure 9 show that the presence of carbon does not have a significant effect on the temperature

of solidification, but does push the precipitation of Laves, δ and σ to later mole fractions of solid (0.89 vs 0.87), which is due to the consumption of Nb by the MC carbides. The step diagrams in Figure 10 through Figure 13 show that the addition of carbon can result in up to 0.8% phase fraction of MC carbide, slightly reduces the amount of σ and δ, and slightly increases the amount of γ'. The step diagrams in Figure 10 through Figure 13 also show that the different AC and AM alloy compositions have negligible difference in equilibrium phase fraction; the AM alloy has slightly more σ and γ' and slightly less δ. Based on the Scheil and step diagrams, it is concluded that, for homogenization, the only major effect of carbon content is to provide a new phase, MC carbide, which is stable at the homogenization heat treatment temperature.

The step diagrams, Figure 10 through Figure 13, along with the phase diagram, Figure 6, are used for determination of the homogenization heat treatment temperature. From the step diagrams, it is seen that the equilibrium phases above 1,060°C through 1,180°C are only γ and MC carbide. From the phase diagram, it is seen that the eutectic reaction Liquid to γ + Laves occurs close to 1,200°C. If the samples are heated too quickly at a temperature above the eutectic reaction temperature, then localized liquid would form, which is not preferred. These results indicate that 1,060°C – 1,200°C is the acceptable homogenization heat treatment range. In order to make a final determination of the heat treatment temperature, a literate review is performed. Chlebus et al. found that PBF samples required a higher homogenization heat treatment than that prescribed for wrought or cast Inconel 718 samples [(Chlebus et al. 2015)], which would indicate that the heat treatment should occur closer to the 1,200°C limit. Scheider et al. performed a literature review of PBF homogenization heat treatment temperatures and decided upon 1,080°C for 1.5 hours [(Schneider, Lund, and Fullen 2018)]. The review performed by Scheider et al. provided contradictory data points for comparison: one work reported that even at 1,180°C for 3

hours, the columnar grain structure continued to exist [(Brenne et al. 2016)], while another work reported complete recrystallization after solutionizing at 954°C for 1 hour [(Zhang et al. 2015; Schneider, Lund, and Fullen 2018)]. Recrystallization is useful for achieving isotropic material properties, but also typically precedes grain growth which is detrimental for strength but beneficial for creep resistance. To promote quicker homogenization times, a homogenization heat treatment temperate of 1,180°C is selected, which is in line with the work of Brenne et al. [(Brenne et al. 2016)].

The DICTRA simulations, Figure 14 through Figure 16, based on the EDS scan results, Figure 19, Table 7, and Table 8, are used to determine the homogenization heat treatment durations. The phase diagram in Figure 6 says that the Laves phase ceases to exist at less than ~6% Nb atomic content, which combined with Figure 14 suggests that the cast sample will no longer have Laves phase between 720 seconds and 1,080 seconds (12-18 minutes); however, it should be expected that diffusion will be slower within the Laves phase and therefore the Laves phase will not be fully dissolved in that timeframe in the cast sample. Figure 16 indicates that the Laves phase should be expected to be dissolved by 3.6 seconds in the AM sample; however, as previously mentioned it should be expected that diffusion will be slower within the Laves phase and therefore the Laves phase will not be fully dissolved in that timeframe in the AM sample. Figure 17 indicates that by 20 minutes, the AM sample should be fully homogenized, while the cast sample is significantly segregated. Figure 17 also indicates that at 1 hour, the cast sample should be more segregated than the AM sample at 20 minutes. The results in Figure 18 and Table 6 indicate that this analysis is correct. 20 minutes is selected to give the short term homogenization behavior of the samples, where it is expected that the AM sample will be fully homogenized but the cast sample will be not fully homogenized. 1 hour is selected as a time where the AM sample will still be fully

homogenized, and the cast sample will be almost fully homogenized. 12 hours is selected as a time indicative of the long term, or equilibrium homogenization behavior.

Based on the step diagrams, Figure 10 through Figure 13, it is expected that the equilibrium Nb segregation, which is due only to MC carbides, will be less than 0.8%. The results in Table 6 concur with this prediction; the cast sample is converging to a Nb segregation value of approximately 0.47%, while the AM sample is converging to a Nb segregation value of approximately 0.36%.

4.2 Further Discussion of Experimental Results

Figure 18 shows the homogenization behavior of the cast and AM samples via backscatter SEM. White sections of the SEM image correspond to Nb-rich phases, such as Laves or MC carbide. It is clear in the as-received state (a) and (e), that there is ample segregation. The segregation has the expected character of Nb-poor dendrite cores with Nb-rich interdendritic zones. From the image and scale bar, it can be seen that for the cast sample the dendrite arm spacing (DAS) is approximately 20 μm, while for the AM sample the DAS is approximately 1 μm; this difference indicates that the AM sample has a much higher cooling rate because DAS is related to cooling rate. Raghavan et al. report a DAS of 1.1 μm for their samples, and estimate approximately 10^4°C/s cooling rates [(Raghavan et al. 2017)]. Figure 18 (e) also shows the presence of the melting pools produced in the PBF process; the microstructure in the overlapping regions is different from the non-overlapping regions. (b) and (f) show the homogenization after 20 minutes, which demonstrates that the AM sample is homogenized and only has very small MC carbides, while the cast sample has significant Laves and MC carbides present. The Laves phase can be distinguished

56

from the MC carbides by its irregular shape compared to the cubic MC carbide shape. Further homogenization time in (c), (d), (g), and (h) show that the trends in each sample continue – the cast sample is further homogenized, while the AM sample becomes less homogenized. The AM sample is more homogenized than the cast sample at all times, especially at 20 minutes. The AM sample becomes less homogenized via the growth of MC carbides, while the cast sample becomes more homogenized via the dissolution of the Laves phase. The difference in homogenization behavior is driven by the shorter diffusion distances in the AM samples, and the smaller degree of initial segregation. The eight samples demonstrate that AM parts require shorter homogenization heat treatment times than traditionally manufactured samples.

Figure 19 shows the EDS scan of two representative Laves sections in the cast and AM samples. From the top image, it can be seen that the Laves phase is much more pronounced in the cast sample. The EDS results correspond to the SEM image: there is significantly more Nb segregation over a larger length in the cast sample compared to the AM sample. The lower segregation in the AM sample could be due to the solidification being so rapid that the Nb cannot segregate to the Laves phase as easily as in the slower solidifying cast sample. This smaller, in length and amount, segregation in the AM sample further supports that the homogenization heat treatment for AM samples requires shorter times or lower temperatures than traditional manufacturing methods.

Figure 21 suggests that the MC carbides are not growing significantly in the cast sample while the Laves phase is dissolving, but that the MC carbide grows significantly in the AM samples due to being the only non-γ phase present. The homogenization heat treatment for AM parts should not be 12 hours long, and as such this MC carbide coarsening issue should not be present in manufactured parts.

The IPF images in Figure 22 for the heat treated samples show that there is no preferred grain orientation, but that there is a columnar microstructure for the as-built AM sample. Wang and Chou [(X. Wang and Chou 2017)] found a very strong preferred [101] grain orientation in their AM samples prior to heat treatment. The change from a strong columnar microstructure to equiaxed grains in the AM samples indicate that significant recrystallization has occurred, even by 20 minutes. This hypothesis is further supported by the low GOS values in the heat treated samples in Figure 25. It is hypothesized that the large surface area and aspect ratio of the columnar grains, combined with the high residual stress and high temperature of the heat treatment all result in rapid recrystallization, even without cold work [(Schneider, Lund, and Fullen 2018)].

The average grain size and distribution presented in Figure 23 and Figure 24 indicate that significant grain growth has occurred in both the cast and AM samples. Converting the columnar grains into an equivalent grain size results in an approximately 75 μm initial grain size being reported for the as-built AM sample. The initial grain size in the AM sample is likely close to the 1-40 μm size reported by Wang and Chou [(X. Wang and Chou 2017)], but by 20 minutes the average size has already become ~175 μm. The shift in distribution suggests that further recrystallization occurs in the AM samples at further homogenization time. The cast sample measurements also suggest growth followed by further minor recrystallization. The rapid recrystallization and grain growth of the AM sample further support developing shorter and cooler heat treatment times for AM components.

Very interestingly, Figure 23 shows that while the cast samples continuously grow in average grain size, the AM samples grow initially (within 20 minutes) and then recrystallize more than they grow, resulting is a smaller average grain size. It is hypothesized that there are finely dispersed oxides from the powder that are acting as grain boundary pinners in the AM sample,

while the cast samples have no such oxides. The oxides would be stable at the heat treatment temperature. Additionally, finely dispersed MC carbides at the grain boundaries would also restrict the grain growth.

5.0 Conclusion

In the present work, the effect of homogenization heat treatment at 1,180°C on the phase transformation and grain evolution in cast and AM Inconel 718 samples are investigated by computational modeling and experimental methods. The computational modelling was performed in a CALPHAD framework via Thermo-Calc and the modelling was used to guide the experimental work. Based on the work presented, and the literature review performed, the following conclusions can be made:

Although the samples analyzed herein reached the homogenization temperature quickly, larger, more complex parts will heat more slowly. Additional attention needs to be paid to the heat-up of large, geometrically complex AM parts to ensure a gradient heat treatment is not accidently applied.

Inconel 718 shows significant segregation on solidification with the primary detrimental segregated element being Nb. The segregation is more pronounced in cast samples than in AM samples. The distances between neighboring Nb-rich regions are higher in cast samples than in AM samples, and the level of Nb enrichment in Nb-rich regions is higher in cast samples.

The phase transformation process is different between cast samples and AM samples. The cast samples slowly dissolve Laves phase while MC carbides are present. The AM samples very rapidly dissolve the Laves phase while MC carbides precipitate over time. The highest level of Nb content in the γ phase is within 20 minutes of heat treatment for the AM samples, while the highest level of Nb content in the γ phase is after more than 1 hour of heat treatment for the cast sample.

The EBSD analysis on recrystallization indicates much faster kinetics in the AM samples than in the cast samples. The AM sample shows no grain orientation and no columnar structure

after 20 minutes of heat treatment, which indicates extensive recrystallization. The AM sample shows significant grain growth after 20 minutes of heat treatment, but shrinkage at times longer than 20 minutes. Further heat treating of cast samples shows complex grain behavior suggestive of growth followed by recrystallization. It is hypothesized that finely dispersed oxides provide grain boundary pinning in the AM samples.

Further work should be done to determine the optimum heat treatment strategy for additively manufactured Inconel 718. This work provides guidance on the different phase transformation and grain behavior between cast and AM samples, and demonstrates that there is a clear need for different heat treatments for AM parts.

The crystal structures of four major phases are presented. The renderings are not to scale, but provide information on the relative placement of the atoms in the lattice.

A.1 γ' FCC L1$_2$ Ni$_3$(Ti,Al) Pm3m
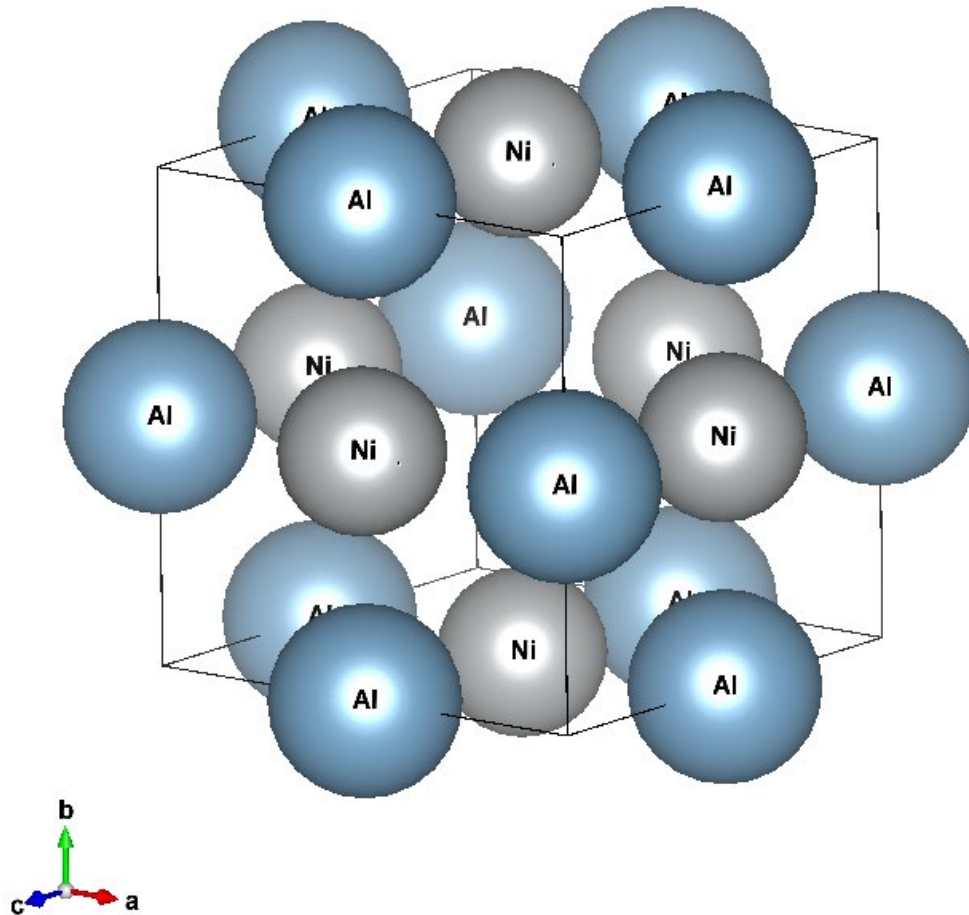
Figure 27 - γ' FCC L12 Ni3(Ti,Al) Pm3m

A.2 γ'' BCT D0$_{22}$ Ni$_3$Nb I4/mmm
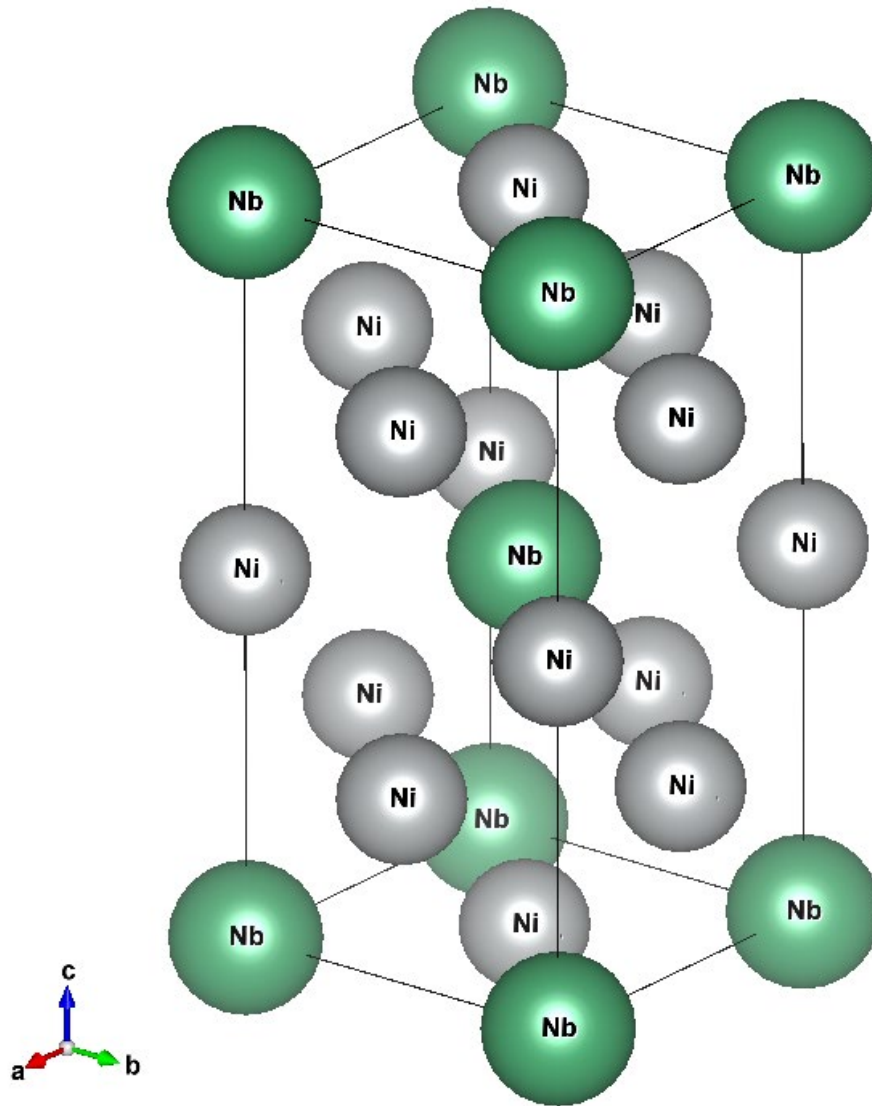
Figure 28 - γ'' BCT D022 Ni3Nb I4/mmm

A.3 δ Orthorhombic D0ₐ Ni₃Nb Pmmn
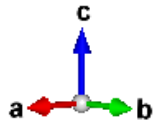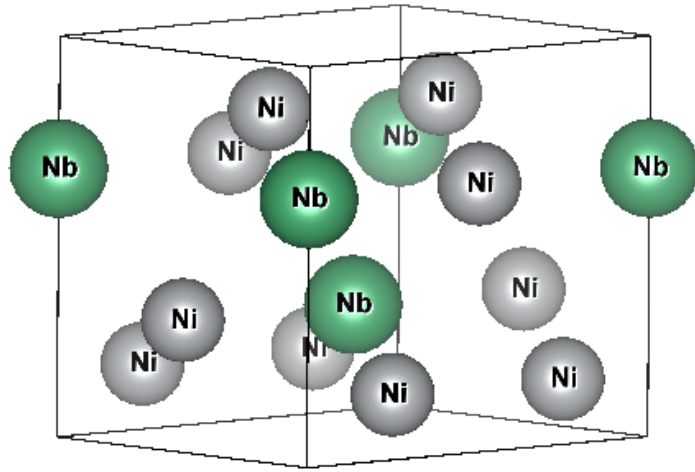
Figure 29 - δ Orthorhombic D0a Ni3Nb Pmmn

A.4 Laves C14 (Ni,Fe,Cr)₂(Nb,Mo,Ti) hP12
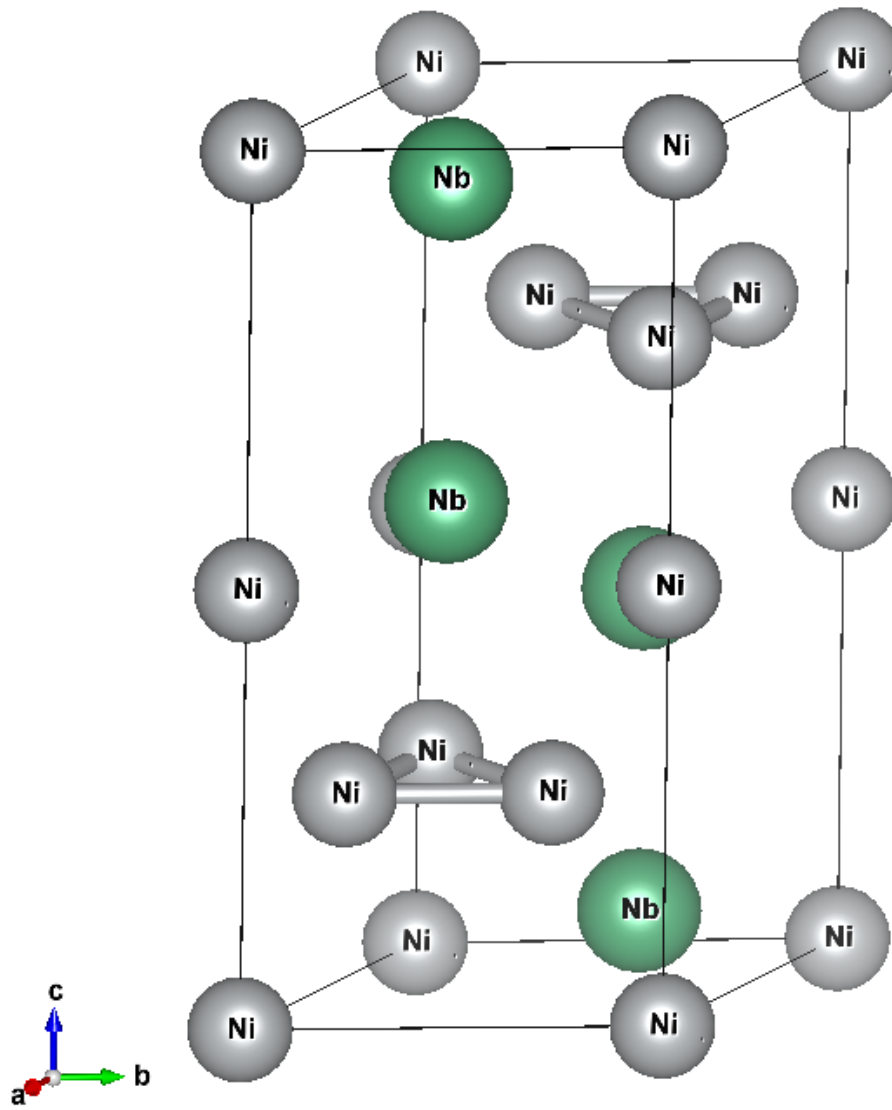
Figure 30 - Laves C14 (Ni,Fe,Cr)2(Nb,Mo,Ti) hP12

Appendix B – EDS Scans

Table 7 - EDS Scan in As-Cast Sample

Point	Distance (μm)	Nb At%	Mo At%	Al At%	Ti At%	Cr At%	Fe At%	Ni At%
1	0	2.7	1.83	0	1.2	21.89	20.05	52.32
2	0.22944	2.49	1.4	0	1.45	21.66	19.7	53.31
3	0.45889	2.53	2.22	0	1.29	21.37	19.98	52.61
4	0.68833	2.16	2.4	2	1.23	21.74	19.46	51.01
5	0.91778	2.58	1.72	2.3	1	20.94	19.44	52.02
6	1.1472	2.11	1.84	1.43	1.25	20.99	20.33	52.04
7	1.3767	2.44	1.87	0	1.26	21.71	19.59	53.13
8	1.6061	2.31	2.07	0	0.97	21.8	20.6	52.24
9	1.8356	2	1.6	0	0.96	22.21	20.59	52.64
10	2.065	1.63	2.29	0	1.11	21.25	20.66	53.06
11	2.2944	1.68	1.8	0	0.95	21.33	21.65	52.59
12	2.5239	2.18	1.61	1.32	0.89	20.4	20.68	52.92
13	2.7533	1.59	1.26	1.52	0.97	20.88	20.83	52.94
14	2.9828	2.01	1.85	0	1.2	21.28	21.18	52.48
15	3.2122	2.02	1.93	1.46	1.07	21.31	19.69	52.51
16	3.4417	2.12	1.73	0	0.98	21.8	20.62	52.76
17	3.6711	1.77	1.76	0	0.93	21.81	20.55	53.17
18	3.9005	1.57	0	0	0.9	21.84	21.61	54.08
19	4.13	1.83	1.76	0	0.71	21.32	21.82	52.55
20	4.3594	1.55	2.2	0	0.96	22.47	20.63	52.19
21	4.5889	2.12	1.83	1.74	0.7	21.77	20.29	51.55
22	4.8183	1.2	1.59	0	0.81	21.94	21.33	53.13
23	5.0478	1.88	1.8	1.73	1	21.54	20.24	51.81
24	5.2772	1.86	2.02	0	1.17	21.92	20.79	52.24
25	5.5067	1.67	1.38	1.56	1.21	21.29	20.25	52.64
26	5.7361	1.83	1.54	1.4	0.71	22.53	19.53	52.46
27	5.9655	2.02	1.97	0	0.84	21.7	21.1	52.36
28	6.195	1.73	2.02	0	1.25	21.98	20.16	52.87
29	6.4244	1.7	1.96	0	0.8	21.79	21.03	52.72

Table 7 (continued)

Point	Distance (μm)	Nb At%	Mo At%	Al At%	Ti At%	Cr At%	Fe At%	Ni At%
30	6.6539	1.3	1.73	0	0.94	21.44	19.96	54.62
31	6.8833	1.59	1.52	0	1.18	22.14	21.37	52.2
32	7.1128	0	1.68	1.98	1.04	22.29	21.6	51.41
33	7.3422	1.66	1.84	0	0.98	22.65	20.3	52.56
34	7.5716	2.09	2.01	1.49	0.87	21.21	20.44	51.89
35	7.8011	2	1.6	0	1.13	21.46	21.23	52.58
36	8.0305	2.01	2.12	0	1.18	21.89	19.99	52.81
37	8.26	1.73	1.82	0	1.2	21.39	20.24	53.62
38	8.4894	1.81	1.54	1.45	1.08	21.38	20.81	51.92
39	8.7189	2.24	1.94	0	1.32	21.54	20.04	52.92
40	8.9483	1.91	1.36	0	1.14	21.22	19.91	54.46
41	9.1778	2.4	1.97	1.52	1.27	21.42	19.62	51.8
42	9.4072	2.16	2.02	1.34	1.24	21.4	19.57	52.28
43	9.6366	2.47	1.91	1.7	0.9	21.46	19.98	51.58
44	9.8661	2.45	1.82	0	1.03	21.4	19.82	53.47
45	10.096	3.05	1.96	0	1.48	21.29	19.2	53.03
46	10.325	3.61	2.14	1.44	1.44	20.98	18.48	51.91
47	10.554	4.16	2.33	1.32	1.5	20.37	18.21	52.11
48	10.784	5.29	1.83	0	1.96	19.98	17.26	53.68
49	11.013	6.89	3.05	0	2.01	19.57	17.37	51.11
50	11.243	9.67	3.25	1.69	1.77	18.24	15.71	49.67
51	11.472	12.17	3.64	0	2.2	17.64	15.44	48.92
52	11.702	14.94	3.77	0	1.77	16.36	14.74	48.43
53	11.931	16.05	3.15	0	2.23	16.82	14.12	47.63
54	12.161	16.83	3.25	0	2.46	16.94	14.33	46.19
55	12.39	13.28	2.89	0	2.45	17.21	14.16	50
56	12.619	9.49	2.76	1.48	2.27	17.08	14.88	52.04
57	12.849	7.13	2.68	1.86	2.25	18.52	16.08	51.47
58	13.078	6.1	2.38	0	2.42	19.07	16.66	53.37
59	13.308	5.74	2.29	1.68	2.18	19.31	17.24	51.55
60	13.537	4.78	2.38	1.7	2.02	19.9	18.2	51.03
61	13.767	4.91	2.44	0	2.15	20.18	16.95	53.38
62	13.996	4.65	1.98	0	2.04	20.54	18.12	52.67
63	14.226	5.5	2.43	1.43	1.95	19.19	17.66	51.84

Table 7 (continued)

Point	Distance (µm)	Nb At%	Mo At%	Al At%	Ti At%	Cr At%	Fe At%	Ni At%
64	14.455	4.84	2.51	0	1.96	20.38	18.04	52.27
65	14.684	4.9	2.62	0	2.05	19.9	18.01	52.52
66	14.914	4.48	2.12	2.53	1.49	19.84	18.47	51.07
67	15.143	3.97	1.6	0	1.78	20.36	19.32	52.97
68	15.373	3.84	2.54	0	1.44	21.13	19.11	51.93
69	15.602	2.99	1.36	1.69	1.23	21.16	19.78	51.8
70	15.832	2.83	2.45	0	1.78	20.76	20.86	51.32
71	16.061	3.07	2.63	1.6	1.43	20.96	18.97	51.34
72	16.291	2.33	2.05	0	1.1	21.74	19.99	52.79
73	16.52	1.57	1.63	0	1.5	20.98	20.91	53.42
74	16.749	1.9	1.78	0	1.05	21.41	20.32	53.54
75	16.979	2.08	1.81	1.49	1.02	21.01	20.56	52.03
76	17.208	1.61	1.67	0	0.99	21.42	21.23	53.08
77	17.438	1.65	2.14	1.66	0.86	21.32	19.39	52.97
78	17.667	1.8	1.63	1.52	0	21.36	20.56	53.13
79	17.897	1.24	1.76	1.76	0.9	21.85	20.43	52.06
80	18.126	1.46	1.81	0	1.15	22.39	20.4	52.79
81	18.356	1.85	1.73	1.53	1.14	21.44	20.21	52.1
82	18.585	1.87	2.13	1.72	1.06	21.13	20.28	51.8
83	18.814	2.04	1.96	1.84	1.04	21.76	20.66	50.7
84	19.044	1.4	1.49	0	1.06	22.04	20.49	53.51
85	19.273	1.81	1.82	1.4	1.22	21.67	20.92	51.17
86	19.503	1.38	1.48	1.38	0.79	21.46	21.01	52.51
87	19.732	1.39	1.38	0	1.07	22.55	20.75	52.86
88	19.962	1.23	1.41	0	0.8	21.94	21.47	53.15
89	20.191	1.1	1.76	1.79	1.01	21.44	20.37	52.54
90	20.421	1.85	1.77	0	0.88	20.82	21.42	53.26
91	20.65	1.84	1.97	0	1.09	21.95	20.81	52.34
92	20.879	1.13	1.67	1.63	0.94	21.57	20.72	52.34
93	21.109	1.88	2.08	1.5	1.22	20.44	20.74	52.14
94	21.338	1.2	1.63	0	0.88	21.86	21.62	52.82
95	21.568	0	1.91	1.45	1	21.29	21.76	52.59
96	21.797	1.39	1.61	0	0.72	22.1	20.64	53.54
97	22.027	1.55	1.7	0	0.91	21.41	21.15	53.27

Table 7 (continued)

Point	Distance (μm)	Nb At%	Mo At%	Al At%	Ti At%	Cr At%	Fe At%	Ni At%
98	22.256	1.4	1.66	1.4	0.8	21.67	21.52	51.56
99	22.486	1.53	0	0	0.8	21.46	22.49	53.72
100	22.715	1.49	1.99	0	0	21.85	20.66	54.02

Table 8 - EDS Scan in As-Built Sample

Point	Distance (μm)	Ni At%	Fe At%	Cr At%	Ti At%	Nb At%	Mo At%	Al At%
1	0	55.46	20.52	22.75	1.27	0	0	0
2	0.042767	51.72	19.93	22.25	2.05	4.06	0	0
3	0.085533	56.41	20.07	22.32	1.21	0	0	0
4	0.1283	50.32	21.21	23.65	1.61	3.22	0	0
5	0.17107	53.65	18.1	23.79	1.65	2.81	0	0
6	0.21383	54.02	18.8	22.89	1.7	2.59	0	0
7	0.2566	52.81	19.43	22.4	1.24	4.12	0	0
8	0.29937	54.12	18.83	23.88	0	3.18	0	0
9	0.34213	54.79	18.46	22.45	1.11	3.2	0	0
10	0.3849	56.95	19.98	21.95	1.12	0	0	0
11	0.42767	52.94	19.66	23.17	1.33	2.9	0	0
12	0.47043	53.02	20.03	22.04	1.75	3.15	0	0
13	0.5132	54.15	20.01	22.68	0	3.15	0	0
14	0.55597	54.32	19.81	22.89	0	2.98	0	0
15	0.59873	52.76	18.39	21.84	0	4.01	3	0
16	0.6415	50.1	19.96	22.07	1.59	3.52	2.77	0
17	0.68426	52.84	19.75	22.64	1.07	3.7	0	0
18	0.72703	55.21	19.49	23.87	1.43	0	0	0
19	0.7698	53.3	19.55	22.13	1.19	3.83	0	0
20	0.81256	54.84	20.07	22.39	0	2.71	0	0
21	0.85533	56.23	20.1	22.52	1.15	0	0	0
22	0.8981	52.76	20.65	22.7	1.01	2.89	0	0
23	0.94086	55.42	20.13	21.74	0	2.71	0	0
24	0.98363	52.15	19.69	23.9	1.23	3.03	0	0
25	1.0264	52.17	19.42	23.91	1.35	3.15	0	0
26	1.0692	53.04	20.81	22.7	0	3.45	0	0
27	1.1119	54.06	20.97	23.56	1.42	0	0	0
28	1.1547	53.17	19.41	22.57	1.18	3.66	0	0
29	1.1975	53.16	20.34	22.21	1.21	3.08	0	0
30	1.2402	56.27	19.92	22.68	1.13	0	0	0
31	1.283	56.95	19.32	22.43	1.3	0	0	0
32	1.3258	55.41	19.9	23.66	1.03	0	0	0
33	1.3685	55.36	19.71	22.14	0	2.8	0	0

Table 8 (continued)

Point	Distance (μm)	Ni At%	Fe At%	Cr At%	Ti At%	Nb At%	Mo At%	Al At%
34	1.4113	54.99	18.81	22	1.41	2.79	0	0
35	1.4541	51.99	20.34	24.3	0	3.37	0	0
36	1.4968	53.56	18.84	23.39	1.03	3.18	0	0
37	1.5396	56.03	19.63	22.78	1.56	0	0	0
38	1.5824	51.95	18.9	22.09	1.16	2.93	2.98	0
39	1.6251	54.31	20.21	22.31	0	3.17	0	0
40	1.6679	53.17	20.63	21.69	1.14	3.38	0	0
41	1.7107	54.24	20.1	22.78	0	2.88	0	0
42	1.7534	53.11	19.03	22.3	1.61	3.95	0	0
43	1.7962	52.38	20.58	22.67	1.21	3.16	0	0
44	1.839	54.74	19.32	21.74	1.27	2.93	0	0
45	1.8817	53.12	19.22	22.38	1.3	3.98	0	0
46	1.9245	54.05	18.4	23.42	1.43	2.7	0	0
47	1.9673	55.62	20.11	22.94	1.33	0	0	0
48	2.01	56.77	19.8	22.38	1.05	0	0	0
49	2.0528	51.81	19.49	22.86	0	3.24	2.6	0
50	2.0956	56.52	19.58	22.36	1.55	0	0	0
51	2.1383	56.55	18.97	23.37	1.11	0	0	0
52	2.1811	54.96	20.86	23.2	0.98	0	0	0
53	2.2239	52.61	19.95	22.57	1.13	3.75	0	0
54	2.2666	56.43	20.13	22.06	1.38	0	0	0
55	2.3094	54.21	19.26	22.39	1.05	3.09	0	0
56	2.3522	55.01	19.16	22.31	0.98	2.54	0	0
57	2.3949	53.98	21.47	23.08	1.47	0	0	0
58	2.4377	53.2	19.69	22.97	1.2	2.95	0	0
59	2.4805	52.14	19.84	23.57	1.32	3.13	0	0
60	2.5232	53.45	20.26	22.04	1.3	2.95	0	0
61	2.566	55.83	19.59	21.32	0	3.26	0	0
62	2.6088	50.02	19.83	23.04	1.46	2.87	2.79	0
63	2.6515	53.41	19.13	22.75	1.47	3.24	0	0
64	2.6943	53.07	21.05	21.54	1.32	3.01	0	0
65	2.7371	54.14	19.48	22.17	1.23	2.98	0	0
66	2.7798	53.42	19.71	22.66	1.12	3.08	0	0
67	2.8226	50.74	18.96	22.64	1.22	3.82	2.62	0

Table 8 (continued)

Point	Distance (μm)	Ni At%	Fe At%	Cr At%	Ti At%	Nb At%	Mo At%	Al At%
68	2.8654	53.62	18.88	23.09	1.23	3.17	0	0
69	2.9081	50.69	20.07	21.78	1.27	3.41	2.78	0
70	2.9509	52.16	19.32	21.32	1.45	3.08	2.67	0
71	2.9937	52.53	20.7	21.95	1.47	3.36	0	0
72	3.0364	53.62	19.22	21.97	1.29	3.9	0	0
73	3.0792	52.48	19.72	23.23	1.73	2.85	0	0
74	3.122	52.76	19.81	22.27	1.61	3.56	0	0
75	3.1647	53.9	19.63	22.03	1.02	3.4	0	0
76	3.2075	53.97	19.89	22.14	1.08	2.93	0	0
77	3.2503	52.19	19.8	23.66	1.24	3.11	0	0
78	3.293	53.14	19.96	22.22	1.1	3.57	0	0
79	3.3358	53.18	19.1	21.99	1.29	4.44	0	0
80	3.3786	53.27	19.47	22.59	1.4	3.27	0	0
81	3.4213	54.28	20.18	21.28	1.32	2.95	0	0
82	3.4641	52.52	19.31	23.22	1.09	3.86	0	0
83	3.5069	54.5	20.63	23.69	1.18	0	0	0
84	3.5496	50.74	18.12	22.69	1.54	4.23	2.68	0
85	3.5924	55.77	18.5	21.12	1.46	3.16	0	0
86	3.6352	48.83	19.27	23.38	1.68	3.87	2.97	0
87	3.6779	54.36	17.93	22.39	1.47	3.85	0	0
88	3.7207	52.61	18.89	22.53	1.51	4.46	0	0
89	3.7635	52.77	18.36	22.57	1.83	4.47	0	0
90	3.8062	51.06	20.68	21.87	1.75	4.64	0	0
91	3.849	53.5	17.27	23.11	1.37	4.75	0	0
92	3.8918	52.39	18.78	22.81	1.23	4.79	0	0
93	3.9345	52.24	19.56	21.04	1.18	5.98	0	0
94	3.9773	51.82	17.93	21.73	1.94	6.58	0	0
95	4.0201	48.67	18.17	20.81	1.43	6.74	4.19	0
96	4.0628	51.06	17.95	22.68	0	8.31	0	0
97	4.1056	51.54	18.4	21.85	0	8.21	0	0
98	4.1484	51.16	18.04	22.37	1.25	7.19	0	0
99	4.1911	51.43	18.87	21.7	1.98	6.03	0	0
100	4.2339	50.49	17.1	23.03	0	5.38	4	0
101	4.2767	54.47	18.34	21.15	1.79	4.25	0	0

Table 8 (continued)

Point	Distance (μm)	Ni At%	Fe At%	Cr At%	Ti At%	Nb At%	Mo At%	Al At%
102	4.3194	51.68	19.27	23	1.19	4.85	0	0
103	4.3622	50.87	19.53	22.2	1.98	5.43	0	0
104	4.405	53.67	18.06	23.06	1.11	4.1	0	0
105	4.4477	51.69	20.74	21.93	1.11	4.53	0	0
106	4.4905	51.3	18.18	21.53	1.15	4.8	0	3.05
107	4.5333	53.75	18.69	22.44	1.14	3.97	0	0
108	4.576	51.16	18.74	21.3	1.52	4.29	2.99	0
109	4.6188	53.93	19.58	20.74	1.35	4.4	0	0
110	4.6616	53.46	20.25	22.28	0	4.02	0	0
111	4.7043	52.27	19.95	22.19	1.93	3.66	0	0
112	4.7471	53.86	18.84	23.26	1.05	2.98	0	0
113	4.7899	53.81	19.69	21.11	1.21	4.17	0	0
114	4.8326	56.94	19.83	23.23	0	0	0	0
115	4.8754	52.66	19.31	22.78	1.53	3.72	0	0
116	4.9182	56.99	19.33	22.7	0.98	0	0	0
117	4.9609	55.25	19.17	21.59	0	3.99	0	0
118	5.0037	54.23	17.9	22.61	1.25	4.01	0	0
119	5.0465	53.93	20	22.16	0	3.92	0	0
120	5.0892	53.21	20	22.18	0.99	3.63	0	0
121	5.132	51.61	19.35	22.49	0	3.94	2.61	0
122	5.1748	52.12	18.88	22.49	0	3.18	3.32	0
123	5.2175	53.14	20.26	22.16	0	4.43	0	0
124	5.2603	53.41	19.47	22.81	1.63	0	2.68	0
125	5.3031	52.88	19.36	23.23	1.72	2.82	0	0
126	5.3458	54.33	19.38	23.5	0	2.79	0	0
127	5.3886	55.88	20.4	22.4	1.32	0	0	0
128	5.4314	52.49	19.61	22.45	1.82	3.62	0	0
129	5.4741	53.55	19.67	22.32	1.31	3.15	0	0
130	5.5169	53.13	17.53	21.19	1.58	3.88	2.69	0
131	5.5597	51.65	19.4	23.7	1.05	4.2	0	0
132	5.6024	51.01	19.45	23.49	1.47	4.58	0	0
133	5.6452	51.97	19.34	22.31	1.21	5.17	0	0
134	5.688	53.03	19.45	21.63	1.79	4.11	0	0
135	5.7307	54.55	18.48	22.91	0	4.05	0	0

Table 8 (continued)

Point	Distance (µm)	Ni At%	Fe At%	Cr At%	Ti At%	Nb At%	Mo At%	Al At%
136	5.7735	51.89	19.63	22.38	1.57	4.53	0	0
137	5.8163	53.03	19.57	21.43	1.62	4.34	0	0
138	5.859	49.77	19.07	22.26	1.42	4.39	3.08	0
139	5.9018	51.88	17.72	21.84	1.43	4.4	2.73	0
140	5.9446	52.04	19.9	22.75	1.37	3.94	0	0
141	5.9873	51.74	19.85	22.7	2.14	3.58	0	0
142	6.0301	53.96	19.28	22.43	0	4.33	0	0
143	6.0729	54.78	20.52	23.52	1.17	0	0	0
144	6.1156	52.59	19.14	22.08	1.69	4.51	0	0
145	6.1584	52.89	20.28	22.61	0	4.22	0	0
146	6.2012	53.55	20.07	22.92	0	3.46	0	0
147	6.2439	52.67	19.69	21.14	1.91	4.59	0	0
148	6.2867	52.75	18.75	22.18	1.95	4.36	0	0
149	6.3295	52.88	19.23	23.33	1.3	3.26	0	0
150	6.3722	55.39	18.68	21.65	0	4.29	0	0
151	6.415	52.09	20.69	22.7	1.57	2.95	0	0
152	6.4578	50.01	19.54	22.25	1.38	3.98	2.84	0
153	6.5005	53.51	19.01	22.77	1.54	3.17	0	0
154	6.5433	54.99	18.61	21.61	1.8	3	0	0
155	6.5861	55.35	18.88	22.85	0	2.91	0	0
156	6.6288	52.1	18.86	23.83	1.27	3.94	0	0
157	6.6716	52.46	18.94	21.33	1.17	3.45	2.66	0
158	6.7144	51.7	18.95	21.66	1.82	2.65	3.21	0
159	6.7571	52.5	19.41	22.29	1.48	4.33	0	0
160	6.7999	52.73	19.55	23.6	1.24	2.88	0	0
161	6.8426	56.9	18.83	24.27	0	0	0	0
162	6.8854	53.92	19.08	22.65	1.62	2.73	0	0
163	6.9282	54.65	19	23.33	0	3.02	0	0
164	6.9709	53.62	19.48	22.64	1.27	2.99	0	0
165	7.0137	54.58	19.01	22.12	1.22	3.07	0	0
166	7.0565	54.5	18.54	22.77	1.18	3.01	0	0
167	7.0992	53.51	22.46	23.05	0.98	0	0	0
168	7.142	51.52	20.8	22.71	1.2	3.77	0	0
169	7.1848	53.83	19.88	22.3	0.95	3.04	0	0

Table 8 (continued)

Point	Distance (µm)	Ni At%	Fe At%	Cr At%	Ti At%	Nb At%	Mo At%	Al At%
170	7.2275	54.39	19.54	22.22	1.19	2.65	0	0
171	7.2703	54.95	19.62	21.1	1.14	3.19	0	0
172	7.3131	54.2	19.59	21.88	1.39	2.93	0	0
173	7.3558	55.07	18.94	21.29	1.24	3.46	0	0
174	7.3986	54.07	19.48	23.69	0	2.75	0	0
175	7.4414	50.98	19.78	21.47	1.89	3.27	2.6	0
176	7.4841	53.02	20.1	21.98	1.15	3.75	0	0
177	7.5269	53.45	20.11	21.89	1.21	3.34	0	0
178	7.5697	54.46	20.03	21.39	1.24	2.88	0	0
179	7.6124	52.89	19.05	21.23	1.27	2.85	2.7	0
180	7.6552	52.08	19.21	22.2	0	3.54	2.96	0
181	7.698	52.57	20.14	22.71	1.6	2.98	0	0
182	7.7407	53.55	19.33	23.19	1.28	2.65	0	0
183	7.7835	52.53	20.3	22.66	1.45	3.05	0	0
184	7.8263	55.5	20.45	22.36	1.69	0	0	0
185	7.869	53.65	18.83	22.48	1.36	3.69	0	0
186	7.9118	51.09	18.04	21.21	1.49	5.07	3.1	0
187	7.9546	53.51	19.65	21.88	1.48	3.48	0	0
188	7.9973	53.34	19.66	21.7	1.3	4.01	0	0
189	8.0401	53.95	18.8	22.09	1.48	3.68	0	0
190	8.0829	53.05	19.14	22.75	0	5.06	0	0
191	8.1256	52.54	19.57	22.19	1.33	4.37	0	0
192	8.1684	54.43	18.96	23.31	0	3.31	0	0
193	8.2112	52.03	19.87	22.83	1.12	4.16	0	0
194	8.2539	53.01	18.96	21.27	0	3.8	2.96	0
195	8.2967	53.51	20.04	23.38	0	3.07	0	0
196	8.3395	53.89	18.39	22.94	1.4	3.38	0	0
197	8.3822	53.54	19.5	22.24	1.65	3.06	0	0
198	8.425	52.84	18.86	23.86	1.31	3.13	0	0
199	8.4678	53.79	19.79	22.81	0	3.62	0	0
200	8.5105	52.94	19.5	23.18	1.29	3.1	0	0

Bibliography

Amato, Krista, Sara Gaytan, Lawrence Murr, Edwin Martinez, P W. Shindo, Jeimmy hernández, S Collins, and Francisco Medina. 2012. "Microstructures and Mechanical Behavior of Inconel 718 Fabricated by Selective Laser Melting." *Acta Materialia* 60: 2229–39. https://doi.org/10.1016/j.actamat.2011.12.032.

Andersson, J. O., Thomas Helander, Lars Höglund, Pingfang Shi, and Bo Sundman. 2002. "Thermo-Calc & DICTRA, Computational Tools for Materials Science." *Calphad: Computer Coupling of Phase Diagrams and Thermochemistry* 26 (2): 273–312. https://doi.org/10.1016/S0364-5916(02)00037-8.

Andersson, Jan Olof, and John Ågren. 1992. "Models for Numerical Treatment of Multicomponent Diffusion in Simple Phases." *Journal of Applied Physics* 72 (4): 1350–55. https://doi.org/10.1063/1.351745.

ASTM. 2018. "ASTM B168-18, Standard Specification for Nickel-Chromium-Aluminum Alloys (UNS N06699), Nickel-Chromium-Iron Alloys (UNS N06600, N06601, N06603, N06690, N06693, N06025, N06045, and N06696), Nickel-Chromium-Cobalt-Molybdenum Alloy (UNS N06617), Nickel-Iron-." West Conshohocken, PA. https://doi.org/10.1520/B0168-18.

Beaubois, V, Julitte Huez, S Coste, Olivier Brucelle, and J Lacaze. 2004. "Short Term Precipitation Kinetics of Delta Phase in Strain Free Inconel 718 Alloy." *Materials Science and Technology* 20: 1019–26. https://doi.org/10.1179/026708304225019830.

Brenne, Florian, A Taube, M Pröbstle, Steffen Neumeier, Dieter Schwarze, Mirko Schaper, and T Niendorf. 2016. "Microstructural Design of Ni-Base Alloys for Hightemperature Applications: Impact of Heat Treatment on Microstructure and Mechanical Properties after Selective Laser Melting." *Progress in Additive Manufacturing* 1. https://doi.org/10.1007/s40964-016-0013-8.

Chen, Q., P. Mason, A. Engström, L. Kjellqvist, Y Du, S. H. Liu, J. Bratberg, A. Markström, and L. J. Zhang. 2016. "The Development and Validation of a New Thermodynamic Database for Aluminum Alloys." *Light Metals 2012*, 291–95. https://doi.org/10.1007/978-3-319-48179-1_50.

Chlebus, E., K. Gruber, T. Kurzynowski, B. Kuźnicka, and J. Kurzac. 2015. "Effect of Heat Treatment on the Microstructure and Mechanical Properties of Inconel 718 Processed by Selective Laser Melting." *Materials Science and Engineering: A* 639: 647–55. https://doi.org/10.1016/j.msea.2015.05.035.

Cozar, R, and Andre Pineau. 1973. "Morphology of y' and y" Precipitates and Thermal Stability of Inconel 718 Type Alloys." *Metallurgical Transactions* 4: 47–59. https://doi.org/10.1007/BF02649604.

Das, Suman. 2003. "Physical Aspects of Process Control in Selective Laser Sintering of Metals." *Advanced Engineering Materials* 5: 701–11. https://doi.org/10.1002/adem.200310099.

Deng, Dunyong, Johan Moverare, Ru Lin Peng, and Hans Söderberg. 2017. "Microstructure and Anisotropic Mechanical Properties of EBM Manufactured Inconel 718 and Effects of Post Heat Treatments." *Materials Science and Engineering: A* 693: 151–63. https://doi.org/https://doi.org/10.1016/j.msea.2017.03.085.

Division, R E N, and Physical Metallurgy. 1981. "A Regular Solution Model for Phases with Several Components and Sublattices, Suitable for Computer Applications." *Journal of Physics and Chemistry of Solids* 42 (2): 297–301. https://ac.els-cdn.com/002236978190144X/1-s2.0-002236978190144X-main.pdf?_tid=498ae0ba-408e-451e-8bf1-95ea572b9e05&acdnat=1530127234_b43e092068cccb0cbf6d6aaf64738523.

Fluke Process Instruments. 2019. "Emissivity - Metals." 2019. https://www.flukeprocessinstruments.com/en-us/service-and-support/knowledge-center/infrared-technology/emissivity-metals.

Gu, D D, W Meiners, K Wissenbach, and R Poprawe. 2012. "Laser Additive Manufacturing of Metallic Components: Materials, Processes and Mechanisms." *International Materials Reviews* 57 (3): 133–64. https://doi.org/10.1179/1743280411Y.0000000014.

Hillert, Mats. 2001. "The Compound Energy Formalism." *Journal of Alloys and Compounds* 320 (2): 161–76. https://doi.org/10.1016/S0925-8388(00)01481-X.

Huang, Xiao, M. C. Chaturvedi, and N. L. Richards. 1996. "Effect of Homogenization Heat Treatment on the Microstructure and Heat-Affected Zone Microfissuring in Welded Cast Alloy 718." *Metallurgical and Materials Transactions A: Physical Metallurgy and Materials Science* 27 (3): 785–90. https://doi.org/10.1007/BF02648966.

Jia, Qingbo, and Dongdong Gu. 2014. "Selective Laser Melting Additive Manufacturing of Inconel 718 Superalloy Parts: Densification, Microstructure and Properties." *Journal of Alloys and Compounds* 585: 713–21. https://doi.org/https://doi.org/10.1016/j.jallcom.2013.09.171.

Keiser, D. D., and H. L. Brown. 1976. "A Review of the Physical Metallurgy of Alloy 718." Springfield, VA.

Kruth, J-P., P Mercelis, J Van Vaerenbergh, L Froyen, and M Rombouts. 2005. "Binding Mechanisms in Selective Laser Sintering and Selective Laser Melting." *Rapid Prototyping Journal* 11 (1): 26–36. https://doi.org/10.1108/13552540510573365.

Kuo, C.-M., Y.-T. Yang, H.-Y. Bor, C.-N. Wei, and C.-C. Tai. 2009. "Aging Effects on the Microstructure and Creep Behavior of Inconel 718 Superalloy." *Materials Science and Engineering: A* 510–511: 289–94. https://doi.org/https://doi.org/10.1016/j.msea.2008.04.097.

Li, Xing, J. J. Shi, C. H. Wang, G. H. Cao, A. M. Russell, Z. J. Zhou, C. P. Li, and G. F. Chen. 2018. "Effect of Heat Treatment on Microstructure Evolution of Inconel 718 Alloy Fabricated by Selective Laser Melting." *Journal of Alloys and Compounds* 764: 639–49. https://doi.org/10.1016/j.jallcom.2018.06.112.

Lukas, Hans Leo, Suzana G. Fries, and Bo Sundman. 2007. *Computational Thermodynamics: The Calphad Method*. University Press, Cambridge: Cambridge University Press.

Ma, Mingming, Zemin Wang, and Xiaoyan Zeng. 2015. "Effect of Energy Input on Microstructural Evolution of Direct Laser Fabricated IN718 Alloy." *Materials Characterization* 106: 420–27. https://doi.org/https://doi.org/10.1016/j.matchar.2015.06.027.

Muggianu, Y M, M Gambino, and J P Bros. 1975. "Enthalpies of Formation of Liquid Alloys Bismuth-Gallium-Tin at 723 °K. Choice of an Analytical Representation of Integral and Partial Excess Functions of Mixing." *J. Chim. Phys. Phys. Chim. Biol.* 72: 83–88.

Osakada, Kozo, and Masanori Shiomi. 2006. "Flexible Manufacturing of Metallic Products by Selective Laser Melting of Powder." *International Journal of Machine Tools and Manufacture* 46 (11): 1188–93. https://doi.org/https://doi.org/10.1016/j.ijmachtools.2006.01.024.

Popovich, V A, E V Borisov, A A Popovich, V.Sh. Sufiiarov, D V Masaylo, and L Alzina. 2017. "Impact of Heat Treatment on Mechanical Behaviour of Inconel 718 Processed with Tailored Microstructure by Selective Laser Melting." *Materials & Design* 131: 12–22. https://doi.org/https://doi.org/10.1016/j.matdes.2017.05.065.

Radhakrishna, CH, and K Prasad Rao. 1997. "The Formation and Control of Laves Phase in Superalloy 718 Welds. Journal of Materials Science, 32(8), 1977–1984. Http://Doi.Org/10.1023/A:1018541915113e Formation and Control of Laves Phase in Superalloy 718 Welds." *Journal of Materials Science* 32 (8): 1977–84. https://doi.org/10.1023/A:1018541915113.

Raghavan, S., Baicheng Zhang, Pei Wang, Chen Nan Sun, Mui Ling Sharon Nai, Tao Li, and Jun Wei. 2017. "Effect of Different Heat Treatments on the Microstructure and Mechanical Properties in Selective Laser Melted INCONEL 718 Alloy." *Materials and Manufacturing Processes* 32 (14): 1588–95. https://doi.org/10.1080/10426914.2016.1257805.

Ram, G. D. Janaki, A. Venugopal Reddy, K. Prasad Rao, and G. Madhusudhan Reddy. 2005. "Microstructure and Mechanical Properties of Inconel 718 Electron Beam Welds." *Materials Science and Technology* 21 (10): 1132–38. https://doi.org/10.1179/174328405x62260.

Redlich, Otto, and A. T. Kister. 2005. "Algebraic Representation of Thermodynamic Properties and the Classification of Solutions." *Industrial & Engineering Chemistry* 40 (2): 345–48. https://doi.org/10.1021/ie50458a036.

Safdar, Shakeel, Andrew J Pinkerton, Lin Li, Mohammed A Sheikh, and Philip J Withers. 2013. "An Anisotropic Enhanced Thermal Conductivity Approach for Modelling Laser Melt Pools for Ni-Base Super Alloys." *Applied Mathematical Modelling* 37 (3): 1187–95. https://doi.org/https://doi.org/10.1016/j.apm.2012.03.028.

Saunders, N., and A. P. Miodownik. 1998. *CALPHAD (Calculation of Phase Diagrams): A Comprehensive Guide*. Edited by N. Saunders and A. P. Miodownik. 1st ed. Pergamon.

Schneider, Judy, Benjamin Lund, and Myles Fullen. 2018. "Effect of Heat Treatment Variations on the Mechanical Properties of Inconel 718 Selective Laser Melted Specimens." *Additive Manufacturing* 21 (February): 248–54. https://doi.org/10.1016/j.addma.2018.03.005.

Slama, C, and M Abdellaoui. 2000. "Structural Characterization of the Aged Inconel 718." *Journal of Alloys and Compounds* 306 (1): 277–84. https://doi.org/https://doi.org/10.1016/S0925-8388(00)00789-1.

Strößner, Johannes, Michael Terock, and Uwe Glatzel. 2015. "Mechanical and Microstructural Investigation of Nickel-Based Superalloy IN718 Manufactured by Selective Laser Melting (SLM)." *Advanced Engineering Materials* 17 (8): 1099–1105. https://doi.org/10.1002/adem.201500158.

Sundararaman, M, P Mukhopadhyay, and Surjo Banerjee. 1992. "Some Aspects of the Precipitation of Metastable Intermetallic Phases in INCONEL 718." *Metall. Trans. A* 23: 2015–28. https://doi.org/10.1007/BF02647549.

Trosch, Tanja, Johannes Strößner, Rainer Völkl, and Uwe Glatzel. 2016. "Microstructure and Mechanical Properties of Selective Laser Melted Inconel 718 Compared to Forging and Casting." *Materials Letters* 164: 428–31. https://doi.org/https://doi.org/10.1016/j.matlet.2015.10.136.

Tucho, Wakshum M., Priscille Cuvillier, Atle Sjolyst-Kverneland, and Vidar Hansen. 2017. "Microstructure and Hardness Studies of Inconel 718 Manufactured by Selective Laser Melting before and after Solution Heat Treatment." *Materials Science and Engineering A* 689 (February): 220–32. https://doi.org/10.1016/j.msea.2017.02.062.

Wang, Xiaoqing, and Kevin Chou. 2017. "Effects of Thermal Cycles on the Microstructure Evolution of Inconel 718 during Selective Laser Melting Process." *Additive Manufacturing* 18: 1–14. https://doi.org/10.1016/j.addma.2017.08.016.

Wang, Xiaoqing, Xibing Gong, and Kevin Chou. 2017. "Review on Powder-Bed Laser Additive Manufacturing of Inconel 718 Parts." *Proceedings of the Institution of Mechanical Engineers, Part B: Journal of Engineering Manufacture* 231 (11): 1890–1903. https://doi.org/10.1177/0954405415619883.

Wang, Zemin, Kai Guan, Ming Gao, Xiangyou Li, Xiaofeng Chen, and Xiaoyan Zeng. 2012. "The Microstructure and Mechanical Properties of Deposited-IN718 by Selective Laser Melting." *Journal of Alloys and Compounds* 513: 518–23. https://doi.org/https://doi.org/10.1016/j.jallcom.2011.10.107.

Wu, K., W. Cao, S. Chen, F. Zhang, and Y.A. Chang. 2012. "A Modeling Tool for the Precipitation Simulations of Superalloys during Heat Treatments," 933–39. https://doi.org/10.7449/2008/superalloys_2008_933_939.

Yadroitsev, I, A Gusarov, I Yadroitsava, and I Smurov. 2010. "Single Track Formation in Selective Laser Melting of Metal Powders." *Journal of Materials Processing Technology* 210 (12): 1624–31. https://doi.org/https://doi.org/10.1016/j.jmatprotec.2010.05.010.

Zhang, Dongyun, Zhe Feng, Chengjie Wang, Weidong Wang, Zhen Liu, and Wen Niu. 2018. "Comparison of Microstructures and Mechanical Properties of Inconel 718 Alloy Processed by Selective Laser Melting and Casting." *Materials Science and Engineering: A* 724 (May): 357–67. https://doi.org/10.1016/J.MSEA.2018.03.073.

Zhang, Dongyun, Wen Niu, Xuanyang Cao, and Zhen Liu. 2015. "Effect of Standard Heat Treatment on the Microstructure and Mechanical Properties of Selective Laser Melting Manufactured Inconel 718 Superalloy." *Materials Science and Engineering A* 644: 32–40. https://doi.org/10.1016/j.msea.2015.06.021.

Zheng, Lei, Guido Schmitz, Ye Meng, Mohammed Chellali, and Ralf Schlesiger. 2012. "Mechanism of Intermediate Temperature Embrittlement of Ni and Ni-Based Superalloys." *Critical Reviews in Solid State and Material Sciences* 37: 181–214. https://doi.org/10.1080/10408436.2011.613492.